UCRL-19263

Cy. 2

STRANGE PARTICLE PRODUCTION IN π^+d INTERACTIONS FROM 1.1--2.4 GeV/c

Donald Wayne Davies
(Ph. D. Thesis)

July 1969

AEC Contract No. W-7405-eng-48

LAWRENCE RADIATION LABORATORY
UNIVERSITY of CALIFORNIA BERKELEY

Cy. 2

UCRL-19263

DISCLAIMER

STRANGE PARTICLE PRODUCTION IN $\pi^+ d$ INTERACTIONS

FROM 1.1 to 2.4 GeV/c

Contents

I. INTRODUCTION

In the fall of 1966 an exposure of 250,000 pictures in the 72 inch chamber was obtained primarily to study ω and η production in the momentum range 1.1-2.4 GeV/c. The results of this part of the experiment will be reported elsewhere. This report is a study of some of the properties of the strange particles produced in this exposure.

Most of the strange-particle states arising from the reaction of a pion with a neutron in the deuteron have been analyzed in the charge-symmetric $\pi^- p$ reaction elsewhere with better statistics. (See Refs. 1 and 2 and papers quoted therein) An exception is $\pi^+ n \rightarrow p K^+ K^-$; this is one of the reactions considered in this report. The reactions on a proton have not been studied with statistics comparable to ours, and we can hope to expand the knowledge of these final states and learn something about the production mechanisms.

In Section II the experimental procedures used in obtaining and reducing the data are described. Section III contains total deuterium cross sections for all final states with one or less unobserved neutral particles. The magnitudes and energy variations of the cross sections are consistent with production off a single nucleon in the deuteron. Three final states are investigated in detail. The $n\Lambda K^+\pi^+$ final state is dominated

by $Y^*(1385)$ production, and this production is well described near threshold by a simple K^* exchange model. The $n\Sigma^+K^o\pi^+$ final state is also analyzed and found to be primarily $n\Sigma^+K^{*+}$. ϕ and $\Lambda(1520)$ production are seen in the ppK^+K^- final state, and the decay distribution of the ϕ indicates that it is produced highly aligned.

II EXPERIMENTAL PROCEDURES.

A. Beam and deuterium properties.

The experiment was performed at the Lawrence Radiation Laboratory Bevatron facility. The deuterium-filled 72-inch bubble chamber was exposed to π^+ mesons from a single-stage separated beam transport system. This system is described in detail elsewhere.[3] For determination of the deuterium index of refraction and range-momentum scale factor see Ref. 4.

B. Scanning and measuring procedure.

The entire exposure was scanned twice for events with a visible neutral decay (vee). A list was made of all events on which the two scans disagreed as to the existence of an event or its event-type; these events were looked at again to resolve the conflict (conflict scan).

The events were measured and fed into the standard Group A three-dimensional reconstruction and kinematic fitting program SIOUX. Events which failed to get an acceptable fit* on the first measurement were remeasured once and twice if they failed the second measurement. After the event had failed three times it was looked at carefully on the scan table and the reason for failure ascertained. If it was not a legitimate event it was deleted from the Master List of events; if it was a legitimate event but unmeasurable for some reason it was so noted. If it was the wrong event-type the event-type was changed and the event remeasured; if there was a small-angle scatter or decay on one of the tracks it was noted and also remeasured.

---

* For a list of which final states were tried for each topology see Group A Memo No. 586, p. 19-27.

C. Scanning efficiency.

With all the checks on the proper event-type (conflict scan, examination of all failing events and operators being able to note wrong event-types) if the event was found at all it was eventually assigned the correct event-type; if it was not a legitimate event it was deleted. Therefore it has been assumed that after this procedure all events have the correct event-type and therefore the scanning efficiency is merely the probability of finding a vee'd event on the film.

Assuming independent probabilities for the two scans we find that the combined scanning efficiency on events which pass our fiducial volume cuts is 99 °/o or greater. The assumption of independent probabilities for the two scans is not necessarily correct; some events might be inherently less visible than others, e.g. vees with the decay plane at a small angle to the camera axis. Losses due to these effects were investigated and found to be negligible in all cases but two-short tracks on vees and Σ^+ decays; for these two cases the remaining events were weighted to account for the loss. See Section E.

D. Exposure size.

The exposure size (events/microbarn) was determined by three different methods:

i) Path length determination.

Ten rolls of film at each momentum were selected and on every fifth frame the numbers of tracks entering and interacting, or leaving the ends or sides of the chamber were recorded. This was used to determine the number of centimeters of

track at each momentum which was then converted to events/microbarn.* These results are given in columns 2 and 3 of table I, where the events/microbarn has been reduced by 3% to account for estimated muon contamination.

ii) Normalization to total cross section.

On these same rolls, on every 25th frame, all interactions were recorded. This was used to give the total number of interactions at each beam momentum (after corrections for events missed - primarily small angle $\pi^+ d \to \pi^+ pn$ with an invisible proton). Comparison with the known $\pi^+ d$ total cross section[5] then gives the events/microbarn. (See column 4 of table I.)

iii) Normalization to a $\pi^- p$ cross section.

The four prongs on the film were scanned and measured, as were the three prongs at all momenta except 1.7 and 1.9 GeV/c. The number of

$$\pi^+ d \to pp\pi^+\pi^-$$
$$pp\pi^+\pi^-\pi^0$$
$$pp\pi^+\pi^-\gamma$$
$$pp\pi^+\pi^-(\text{missing mass})$$

in the three and four-prongs combined was compared to the charge-symetric cross section[6] to $\pi^+ n$:

$$\pi^- p \to n\,\pi^+\pi^-$$
$$\to \pi^+\pi^-\ (\text{missing mass}).$$

After lowering the cross section by 3 % to account for screening of the neutron by the proton we get another,

* 26.3×10^6 cm. of track gives 1 ev/μb.

Table I. Exposure size.

Beam momentum (GeV/c)	Path length cm($\times 10^6$)	Events/microbarn i	ii	iii	"average"
1.12	12.00	0.44	0.42 ± .01	0.38 ± .04	0.43
1.30	11.4	0.42	0.43 ± .01	0.44 ± .04	0.43
1.53	68.0	2.51	2.57 ± .07	2.4 ± .2	2.53
1.58	12.4	0.46	0.46 ± .01	0.47 ± .05	0.46
1.70	78.0	2.88	2.97 ± .07		2.91
1.86	78.1	2.87	2.92 ± .06		2.90
2.15	83.2	3.07	2.88 ± .06	3.2 ± .3	2.93
2.37	25.9	0.96	0.84 ± .02	1.0 ± .1	0.93

though less accurate, estimate of the events/microbarn. See column 5 of table I.

The last column in table I gives the exposure size used to calculate the cross sections.

E. Detection corrections.

If a K^0 or a Λ is produced near the bubble chamber walls there is a chance it will decay outside the visible region and be lost. Also if it decays too close to the production vertex it will appear to be a non-vee event and also be lost. In order to correctly account for losses due to these effects fiducial volume restrictions were imposed on the events. Events which had a vee near one of the walls were flagged and treated as if they had never been found. It was determined that events with decay vertices closer than 6 mm to the production vertex also were missed. Therefore all events with neutral decay lengths less than 6 mm were also flagged and treated as if never found.

When a Λ of laboratory momentum 120 MeV/c decays with the proton going backward in the Λ rest frame, the proton is at rest in the laboratory. Also if the Λ is very low momentum in the laboratory, the vee will have a very large opening angle and will be mistaken for a stray track. We therefore have a loss of low momentum Λ's. If the Λ has 800 MeV/c momentum and the π^- goes backward a similar situation occurs - the π^- is very low momentum and interacts or decays before going very far. Fig. 1(a) shows this effect. The loss of events was parameterized by the function shown in fig. 1(b).

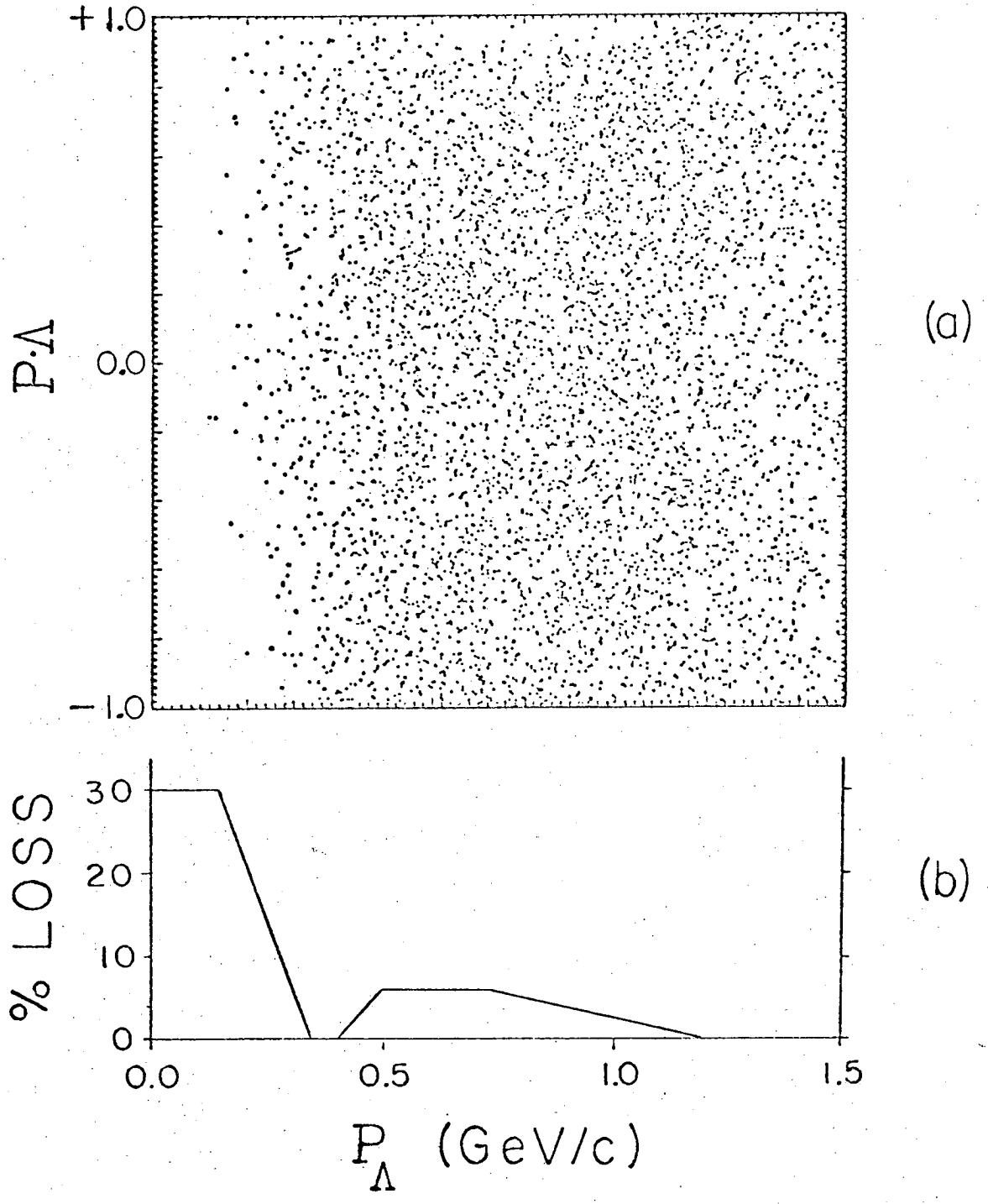

Fig. 1 a) Scatter plot of the decay cosine of the Λ with respect to its line of flight versus the Λ laboratory momentum.

b) Loss of events as a function of Λ laboratory momentum.

The Σ^+'s produced in this experiment typically have over 1 GeV/c laboratory momentum. If the Σ^+ decays into $p\pi^0$ the proton makes a small angle with respect to the Σ^+ line-of-flight ($<15^o$) and also has little change in ionization density. Under these circumstances the scanners have difficulty identifying the event as a charged decay instead of a proton scatter. Therefore, for purposes of cross section calculation, we have used only the $n\pi^+$ decay mode of the Σ^+ and corrected the number of events to account for the $p\pi^0$ mode. The $n\pi^+$ events were also weighted to try to account for low momentum π^+'s (as in Λ decay) and scanning losses for high momentum colinear decays. The correction for these latter two was taken as 30%. Because of uncertainties in this procedure there could be systematic errors of the order of 20 o/o in the cross sections for final states containing Σ^+'s.

The events which passed the fiducial volume tests were weighted to account for these losses. For an observed neutral decay the weight was

$$W = \left[\left(e^{-\tau_c/\tau} - e^{-\tau_f/\tau}\right)(1 - f)\right]^{-1},$$

for an unobserved neutral decay

$$W = \left[1 + \frac{br}{1-br}\left(e^{-\tau_f/\tau} + \left(e^{-\tau_c/\tau} - e^{-\tau_f/\tau}\right)(f)\right)\right]^{-1},$$

and for an observed charged decaying particle

$$W = \left[e^{-\tau_c/\tau}\right]^{-1},$$

where τ is the particle mean lifetime, τ_f is the proper time for the particle to get to the fiducial volume walls, τ_c is the proper time to go the minimum length (6 mm), br is the branching fraction into $p\pi^-$ for

a Λ and $\pi^+\pi^-$ for a K_S (taken as 2/3 in each case) and f is the function shown in fig. 1(b) for a Λ and is zero for a K_S.

F. Separation of hypotheses

For each hypotheses that had an acceptable fit a "badness" function was constructed.

$$B = \chi^2_k - 5*N_k + \tfrac{1}{2}(\chi^2_I - N_I) - F_{kL}$$

where χ^2_k is the kinematic chisquared, N_k is the number of kinematic constraints, χ^2_I and N_I are the same for the track ionization density, and $F_{kL} = 0$ for a Λ, or $F_{kL} = 10$ for a K_S. See Ref.(7) for a description of the ionization chisquared routine. Approximately one-third of the events had passing measurements on the Spiral Reader measuring machine, and therefore had ionization information.

Because of the decay kinematics it is possible for most Λ's to pass as K_S's, but very few K_S decays can fake a Λ. (Because of the higher Q-value for K_S decay, the K_S tends to have a much larger opening angle in the laboratory than a Λ). Therefore we chose to bias against the K_S fits; a factor of 10 added to the "badness" of the K_S fit was found to produce essentially perfect Λ-K_S separation.

The hypothesis with the lowest badness was tentatively accepted as the "best" fit. If there was any other hypothesis which had a badness within 10 of the best fit, and if it was possible to distinguish between the two hypotheses on the basis of track ionization, the event was looked at on the scan table. Any hypotheses which were inconsistent with the observed ionization were killed.

III. ANALYSIS AND RESULTS

A. Cross sections

It is not necessary (or even possible in some cases) to do a separation on an event-by-event basis to get the cross section; all that is required is the number of events that should be assigned to each hypothesis. The cross sections were determined in the following way. Final states with the same visible particles were lumped together (e.g. $[n\Lambda K^+\pi^+$ and $n\Sigma^o K^+\pi^+]$ or $[p\Lambda K^+$, $p\Sigma^o K^+$, $p\Lambda K^+\pi^o$, and $p\Sigma^o K^+\pi^o]$, etc.). Mass and angular distributions for these events were then examined to determine how many ambiguous events to assign to one or the other final states. Two examples will serve as illustrations:

i) Many of the final states in this experiment are one-constraint (one missing non-decaying neutral) with a decaying Λ. The corresponding missing-mass (zero-constraints) hypothesis is the same final state with the Λ replaced by a Σ^o; which means that we are now missing the original neutral plus a γ-ray. However, any event with a low energy γ-ray will have a perfectly acceptable one-constraint fit, making it impossible to tell the two hypotheses apart. Therefore to get the correct number of one and zero-constraint events the missing-mass distributions for events with a best fit to either the one-constraint or the zero-constraint hypothesis were plotted together and the number of one-constraint events estimated. See fig. 2 for an example of this procedure.

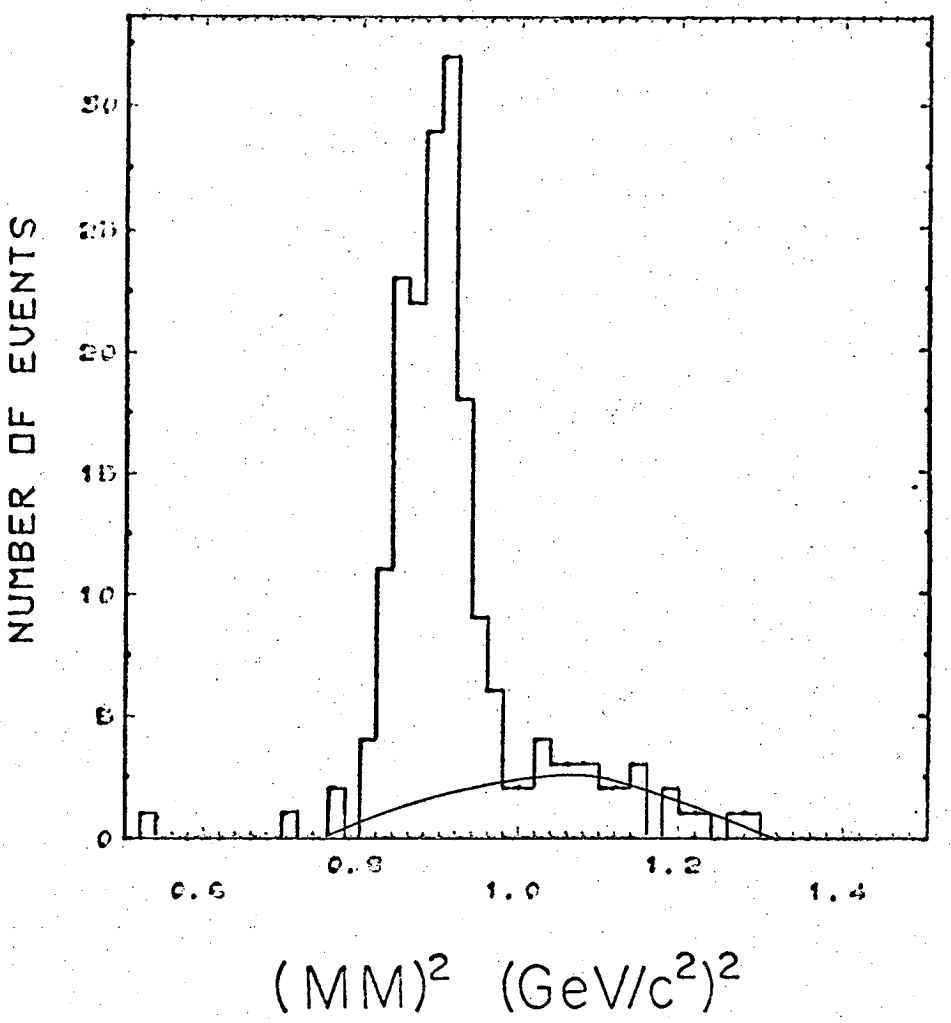

Fig. 2 Missing mass squared for events with a best fit to $n\Lambda K^+\pi^+$ or $(n\gamma)\Lambda K^+\pi^+$. The missing mass distribution for $(n\gamma)\Lambda K^+\pi^+$ was assumed to be of the shape given by the curve.

ii) The states $p\Lambda K^+$ (four-constraint) and $p\Sigma^o K^+$ (two-constraint) were also impossible to distinguish on an event-by-event basis. When the Σ^o decays with the γ-ray going backwards along the line of flight of the Σ^o, the γ-ray has very little laboratory momentum and energy and it becomes difficult (because of the measurement errors) to tell it from no particle at all-i.e. a $p\Lambda K^+$ event. When the proton has a laboratory momentum less than about 80 MeV/c it does not go far enough ($\sim$2 mm.) to leave a visible track and this in effect adds on another 50 MeV/c or so in a random direction to the measurement error. Under these circumstances it is impossible to tell a Σ^o with a backward-going γ-ray from a Λ event. The "badness" function biases rather strongly in favor of the four-constraint fit and therefore events with a soft γ-ray will preferentially be called Λ events. Fig. 3 (a, b) shows the Σ^o decay distributions for events with a "best" fit to a Σ^o hypothesis; in the odd-prongs (events with an invisible proton), the loss of events with backward-going γ-rays is especially conspicuous. This distribution was plotted for each beam momentum and used to determine how many Σ^o events had been called Λ's.

The cross sections determined in this way are given in table II and figs. 4-16. Errors quoted take into account uncertainties in separating different final states; the cross sections quoted for final states containing a Σ^+ could have an additional 20 $^o/_o$ systematic error. (See Section E.)

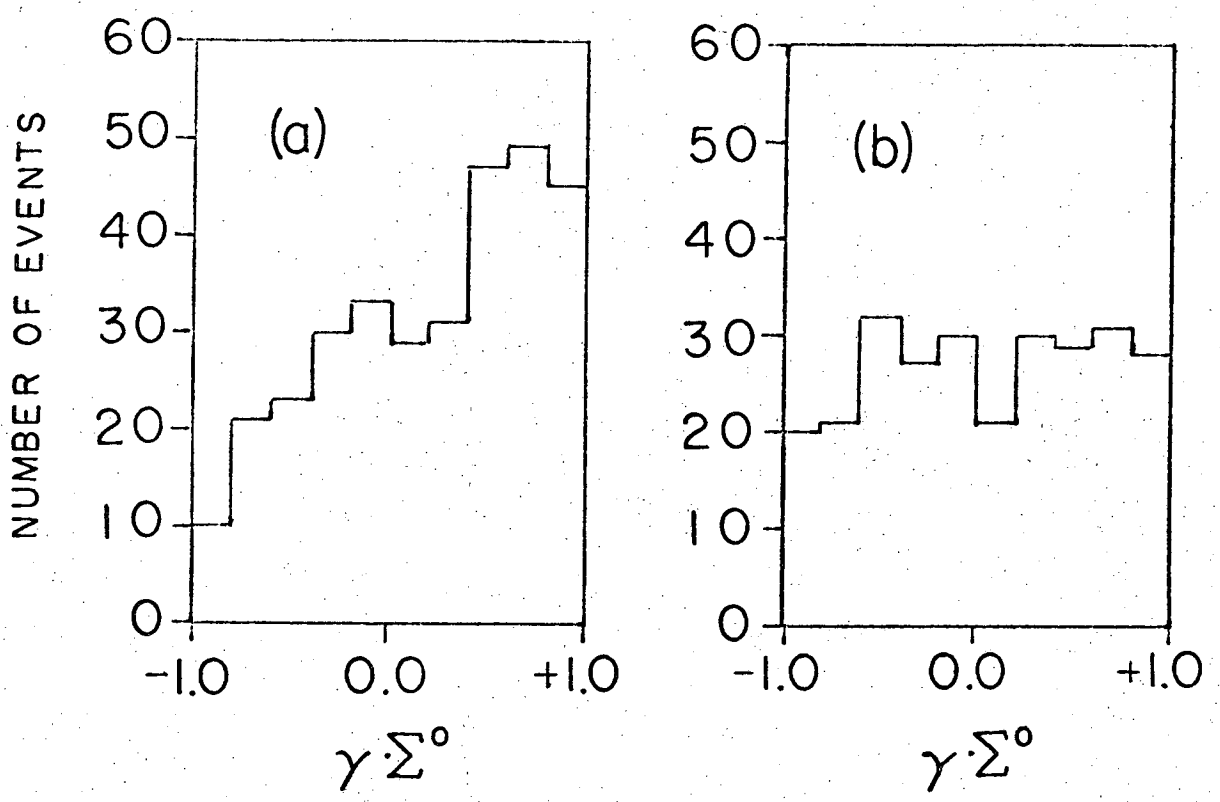

Fig. 3 Distribution of the γ-ray in the Σ^0 rest frame with respect to the Σ^0 line of flight. a) odd prong events (events with an invisible proton) b) even prong events (events with a visible proton)

Table II. Total cross sections (μb)

Final state	Beam momentum (GeV/c) 1.12	1.30	1.53	1.58	1.70	1.86	2.15	2.37
$p\Lambda K^+$	368 ± 55	475 ± 55	292 ± 20	248 ± 50	246 ± 20	167 ± 25	121 ± 25	101 ± 30
$p\Sigma^o K^+$	149 ± 45	178 ± 45	132 ± 18	135 ± 40	106 ± 15	152 ± 27	114 ± 25	77 ± 25
$p\Sigma^+ K^o$	39 ± 39	254 ± 90	234 ± 45	270 ± 90	188 ± 39	174 ± 33	142 ± 33	52 ± 33
$p\Lambda K^+\pi^o$			79 ± 10	89 ± 22	114 ± 9	131 ± 9	151 ± 12	150 ± 22
$p\Lambda K^o\pi^+$		9 ± 7	69 ± 7	73 ± 18	84 ± 7	104 ± 8	160 ± 10	126 ± 17
$p\Sigma^o K^o\pi^+$			21 ± 11	0 ± 18	19 ± 9	34 ± 10	55 ± 15	74 ± 29
$n\Lambda K^+\pi^+$		11 ± 7	72 ± 12	65 ± 22	108 ± 12	134 ± 14	118 ± 12	67 ± 16
$n\Sigma^+ K^o\pi^+$					7 ± 15	62 ± 21	110 ± 26	160 ± 60
ppK_SK_L			1.9± 1.2	0.0± 4.0	17.5± 3.5	18.6± 3.5	28.6± 4.5	18.7± 7.5
ppK_SK_S					6.2± 3.1	8.4± 3.5	13.2± 5.1	5.2± 5.2
$pnK^+\bar{K}^o$			4.0± 2.8	11 ± 11	20 ± 6	25 ± 6	48 ± 9	67 ± 18
$p\Lambda K^+\pi^+\pi^-$					10 ± 3	18 ± 4	47 ± 7	58 ± 15
$p\Lambda K^o\pi^+\pi^o$					3.3± 3.3	9.7± 5.5	28 ± 10	63 ± 24

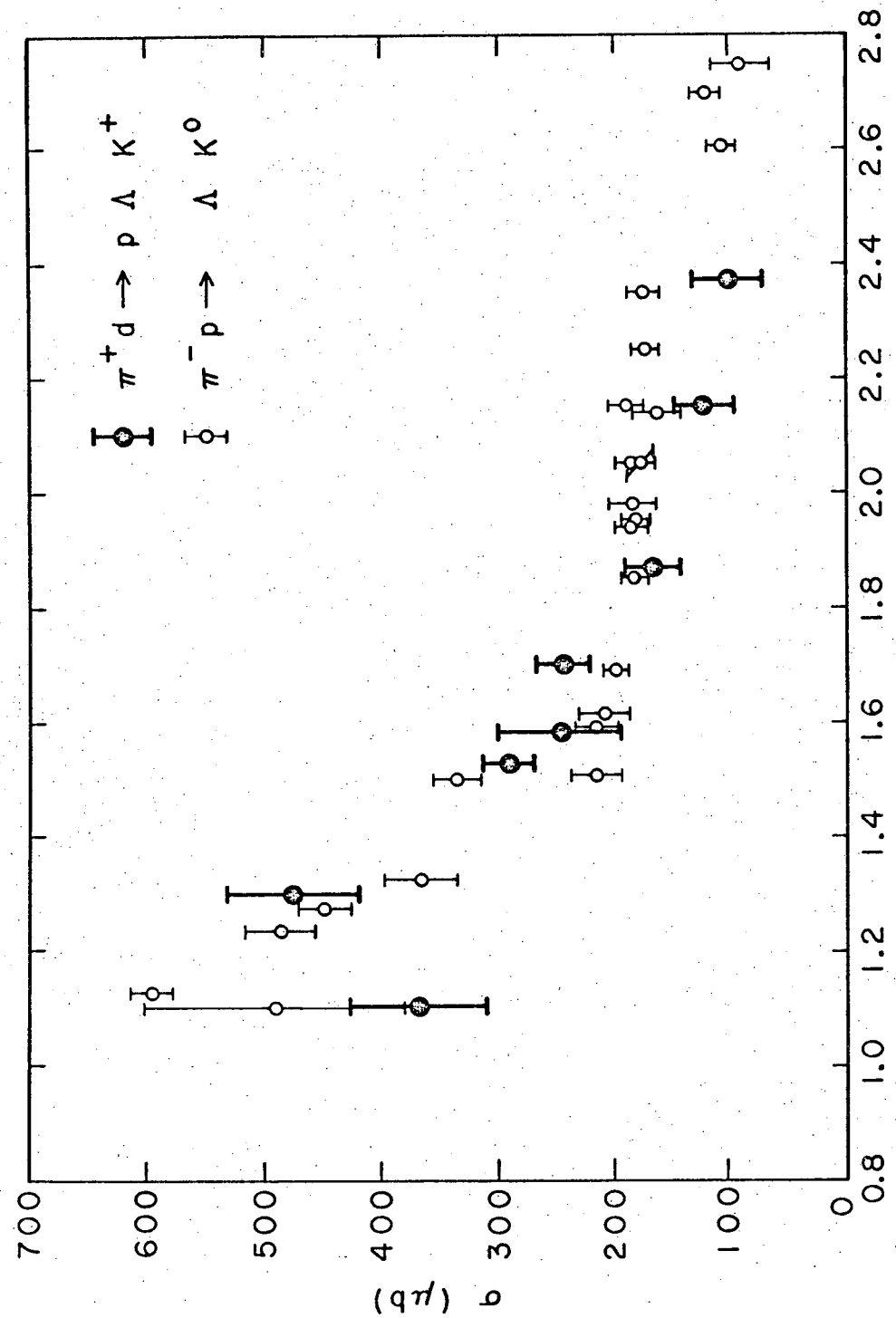

Fig. 4 Total cross section as a function of incident momentum for $p\Lambda K^+$ final state from this experiment (filled points), and ΛK^o final state from Refs. 1 and 2 and papers quoted therein (open points).

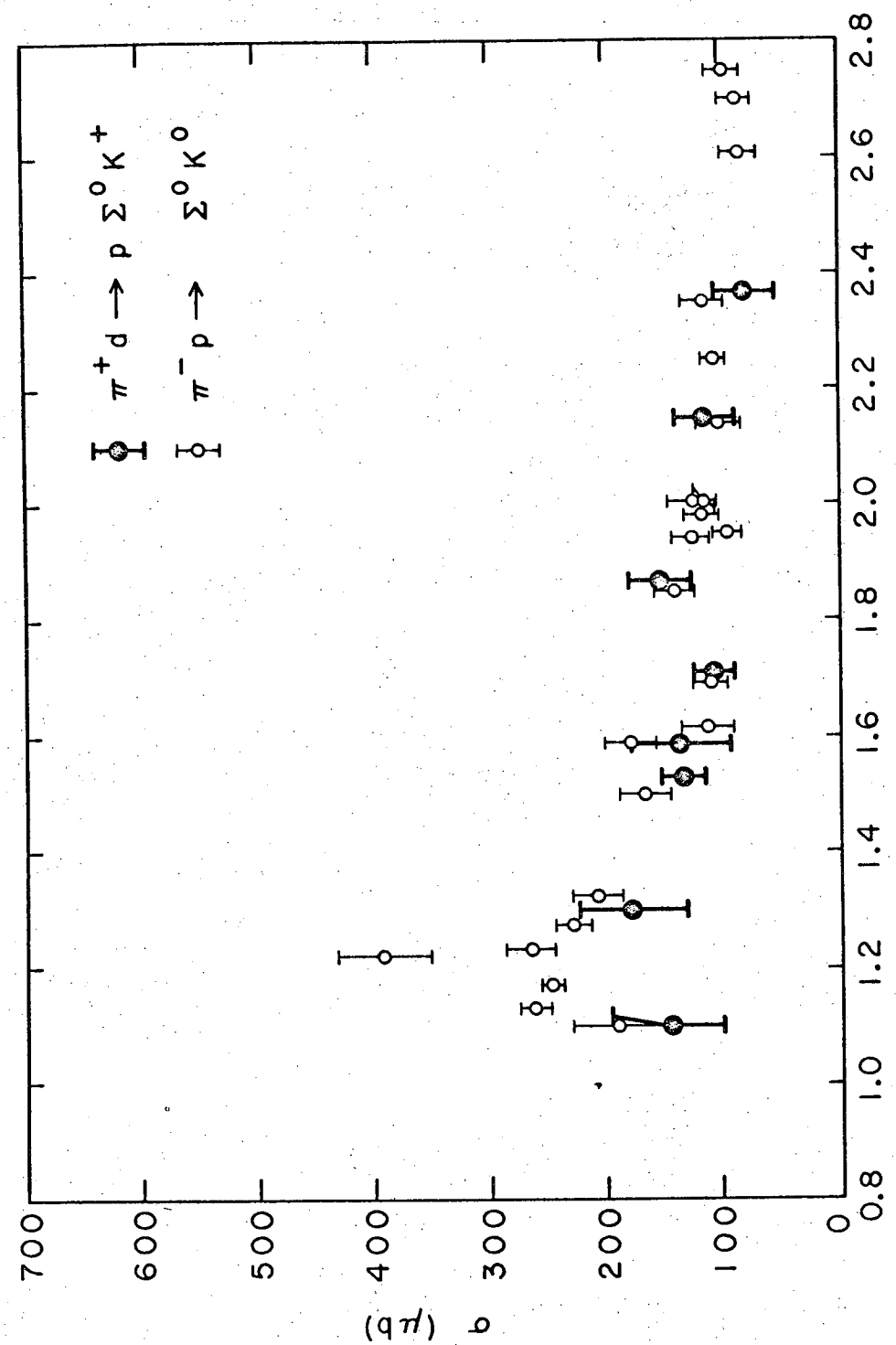

Fig. 5 Total cross section as a function of incident momentum for $p\Sigma^0K^+$ final state from this experiment (filled points), and Σ^0K^0 final state from Refs. 1 and 2 and papers quoted therein (open points).

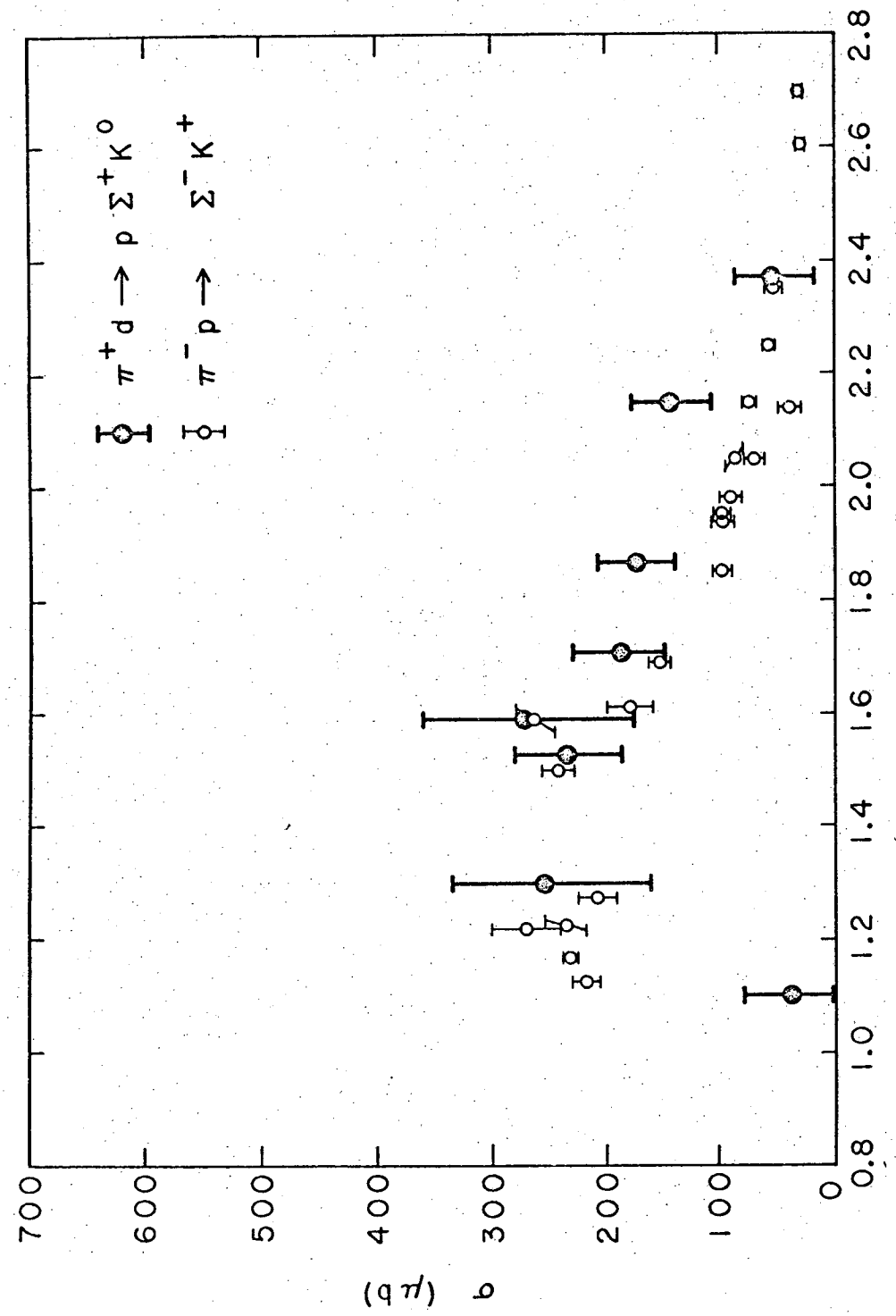

Fig. 6 Total cross section as a function of incident momentum for $p\Sigma^+K^o$ final state from this experiment (filled points), and Σ^-K^+ final state from Refs. 1 and 2 and papers quoted therein (open points).

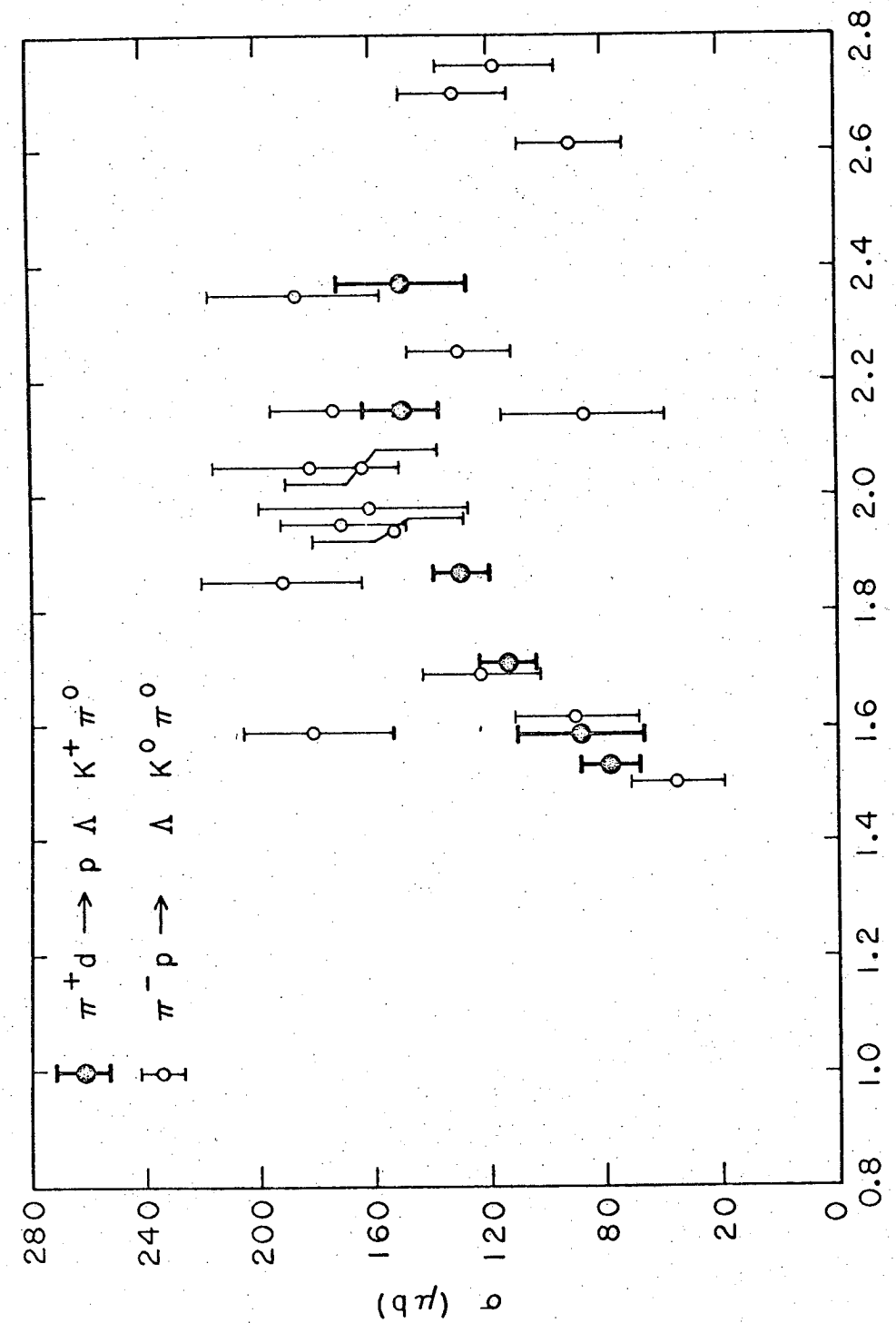

Fig. 7 Total cross section as a function of incident momentum for $p\Lambda K^+\pi^o$ final state from this experiment (filled points), and $\Lambda K^o\pi^o$ final state from Refs. 1 and 2 and papers quoted therein (open points).

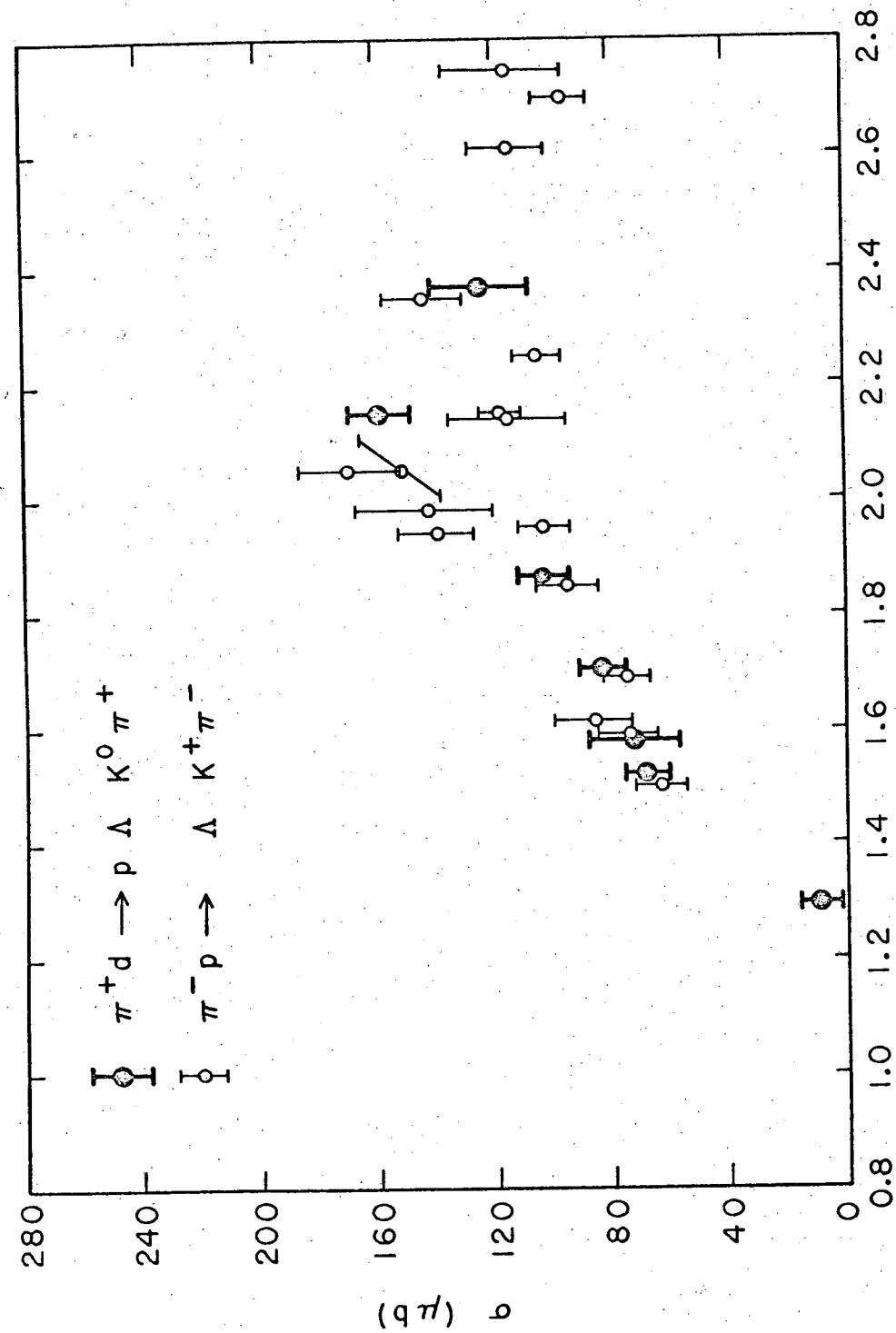

Fig. 8 Total cross section as a function of incident momentum for $p\Lambda K^o \pi^+$ final state from this experiment (filled points), and $\Lambda K^+ \pi^-$ final state from Refs. 1 and 2 and papers quoted therein (open points).

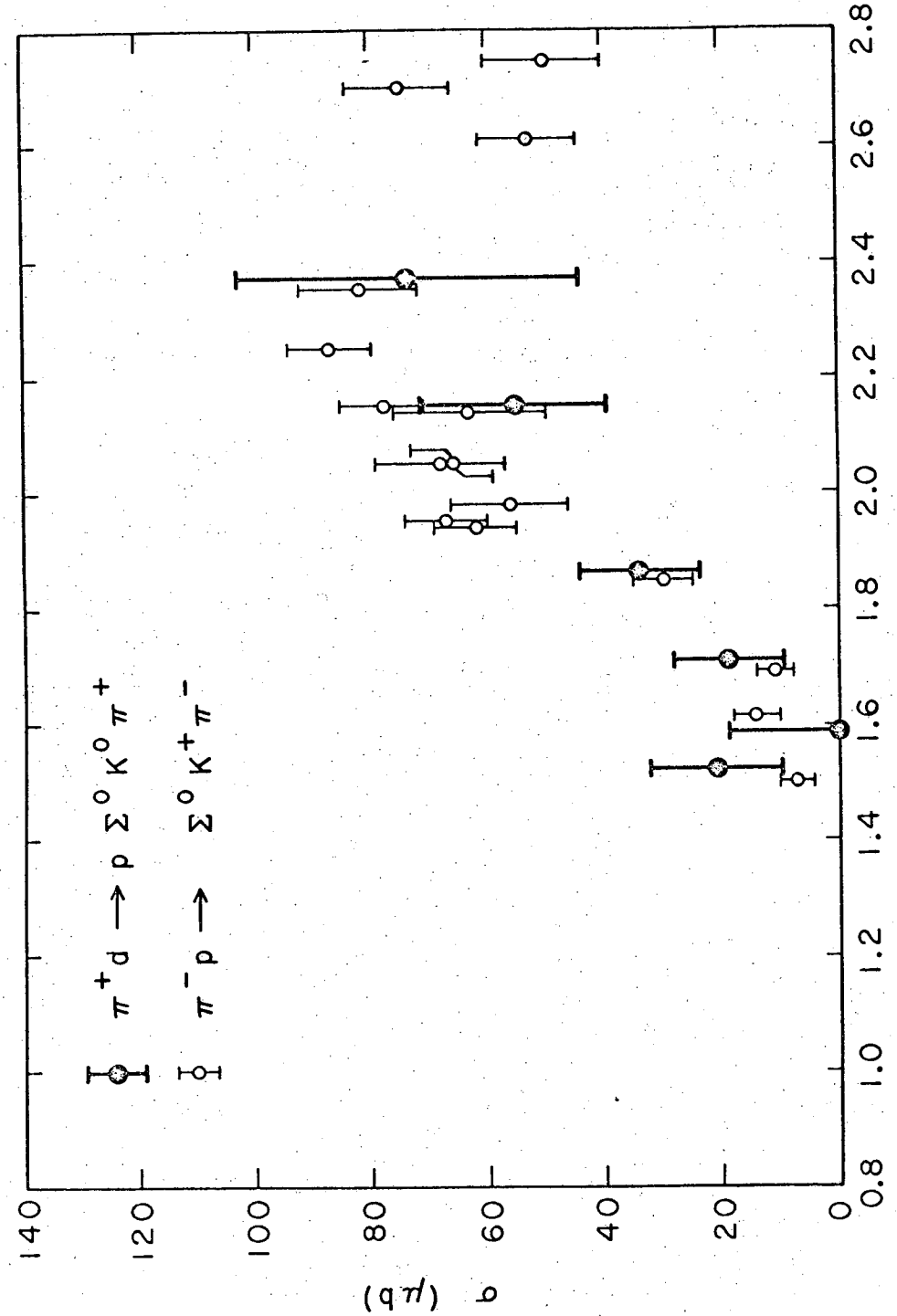

Fig. 9 Total cross section as a function of incident momentum for $p\Sigma^0K^0\pi^+$ final state from this experiment (filled points), and $\Sigma^0K^+\pi^-$ final state from Refs. 1 and 2 and papers quoted therein (open points).

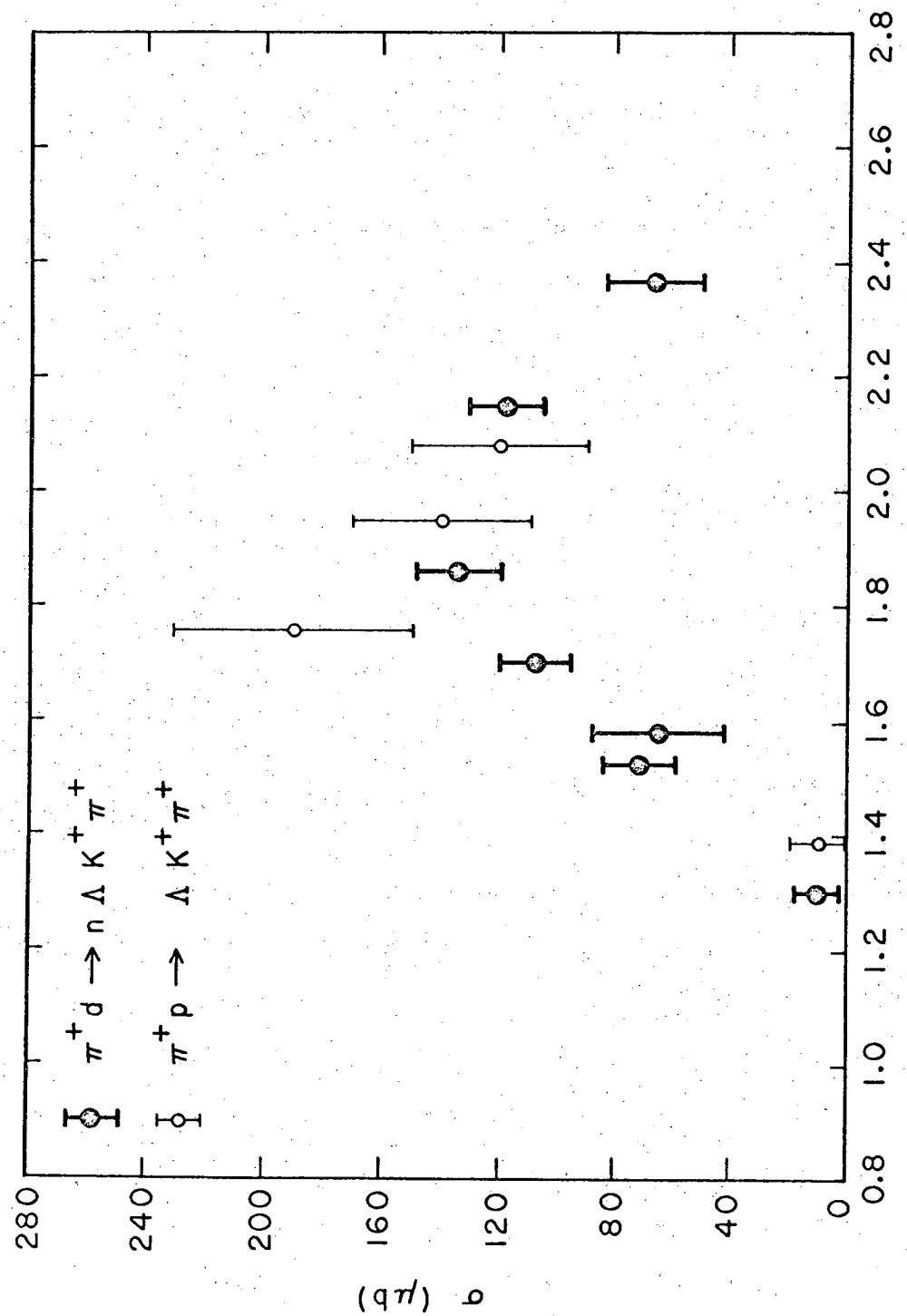

Fig. 10 Total cross section as a function of incident momentum for $n\Lambda K^+\pi^+$ final state from this experiment (filled points), and $\Lambda K^+\pi^+$ final state from Refs. 8 and 9 (open points).

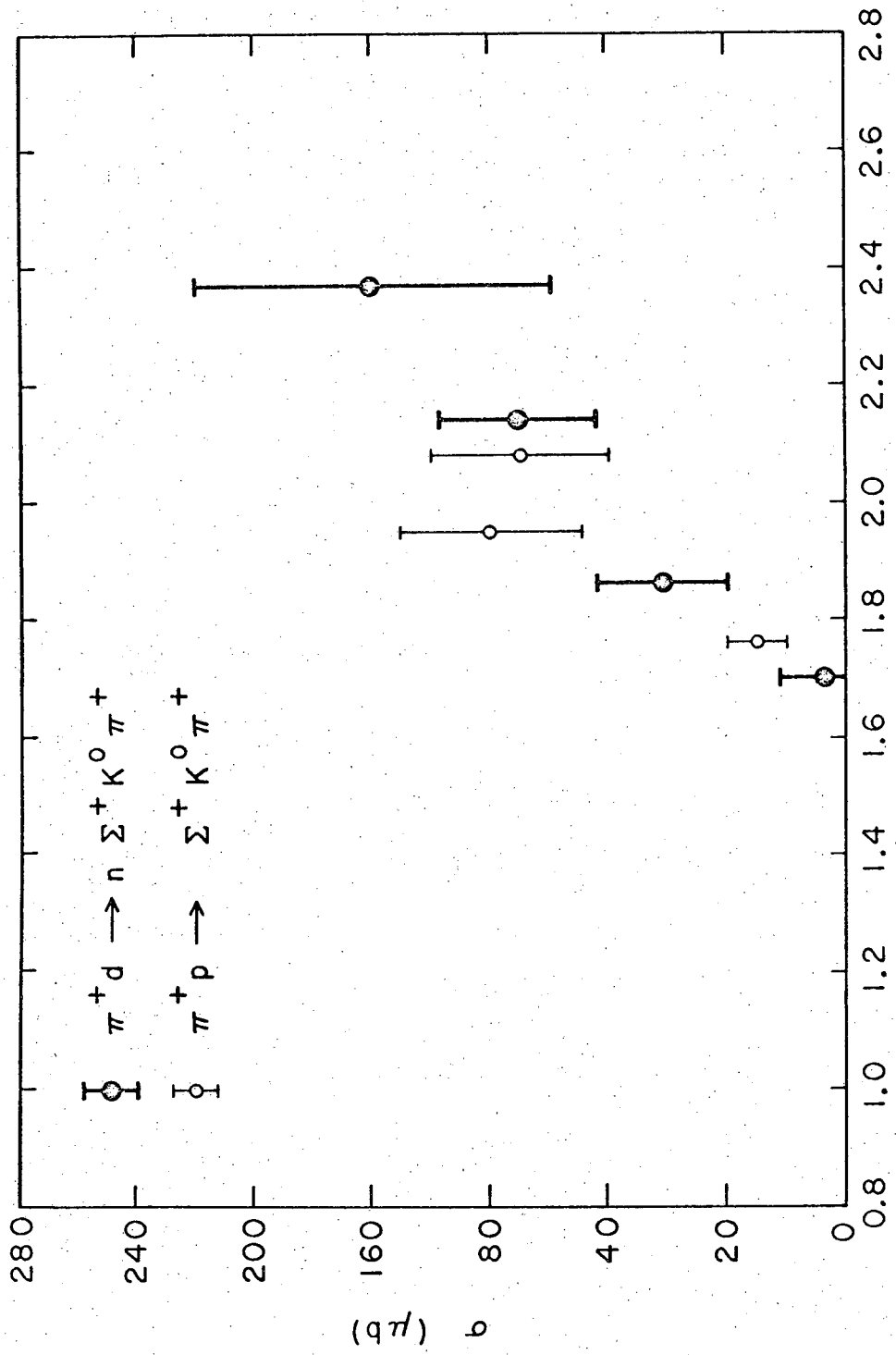

Fig. 11 Total cross section as a function of incident momentum for $n\Sigma^+K^o\pi^+$ final state from this experiment (filled points), and $\Sigma^+K^o\pi^+$ final state from Refs. 8 and 9 (open points).

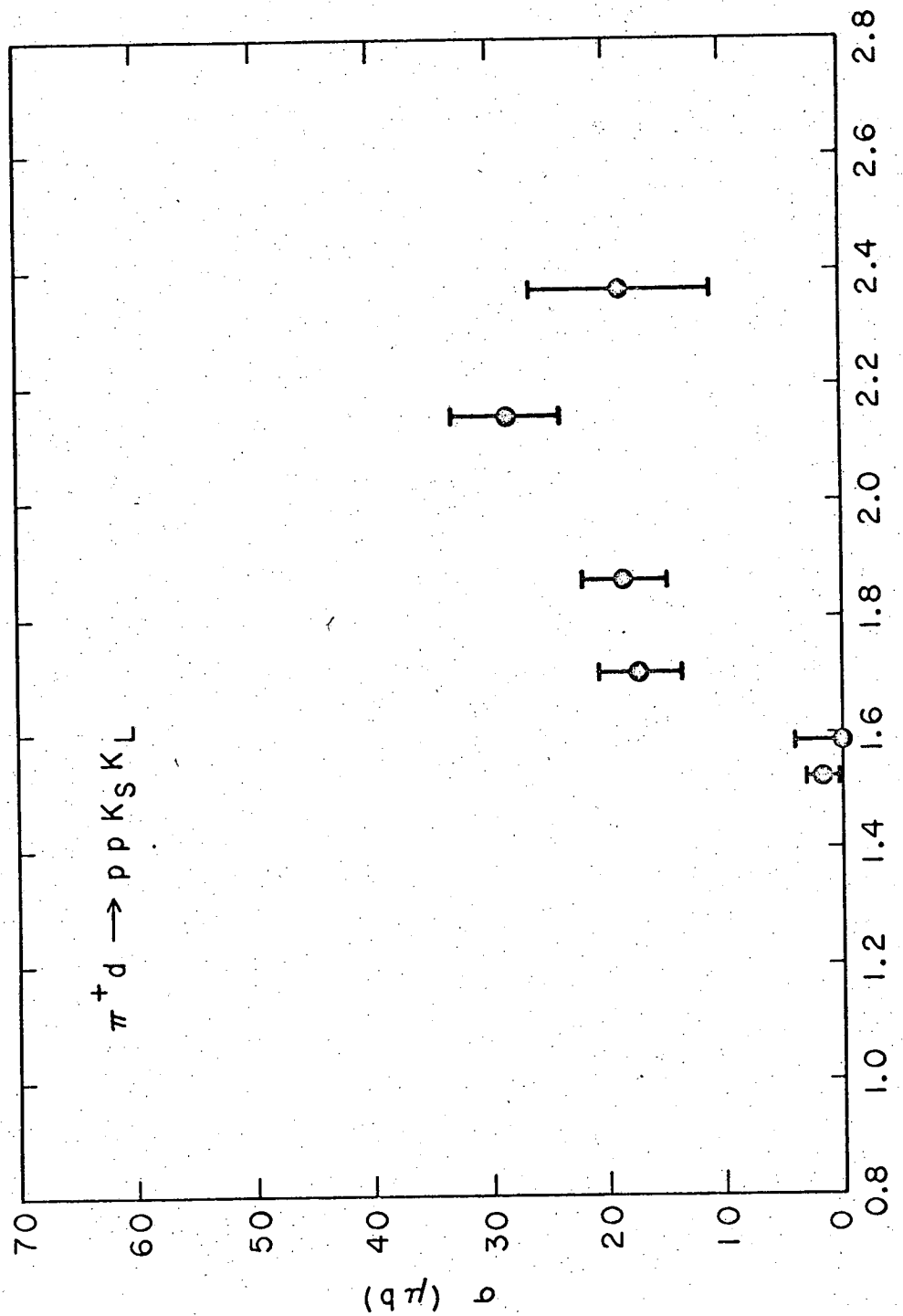

Fig. 12 Total cross section as a function of incident momentum for ppK_SK_L final state .

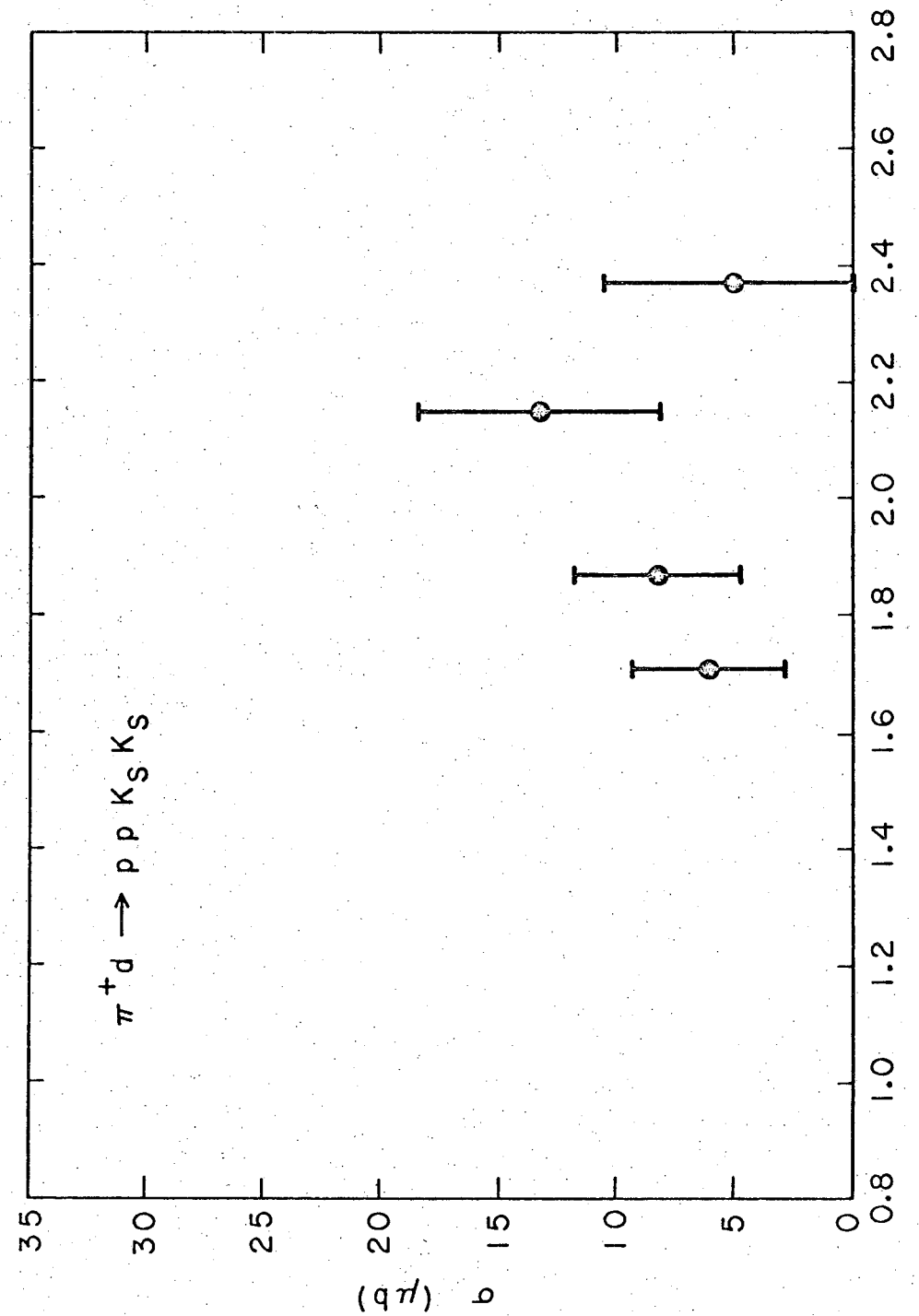

Fig. 13 Total cross section as a function of incident momentum for ppK_SK_S final state.

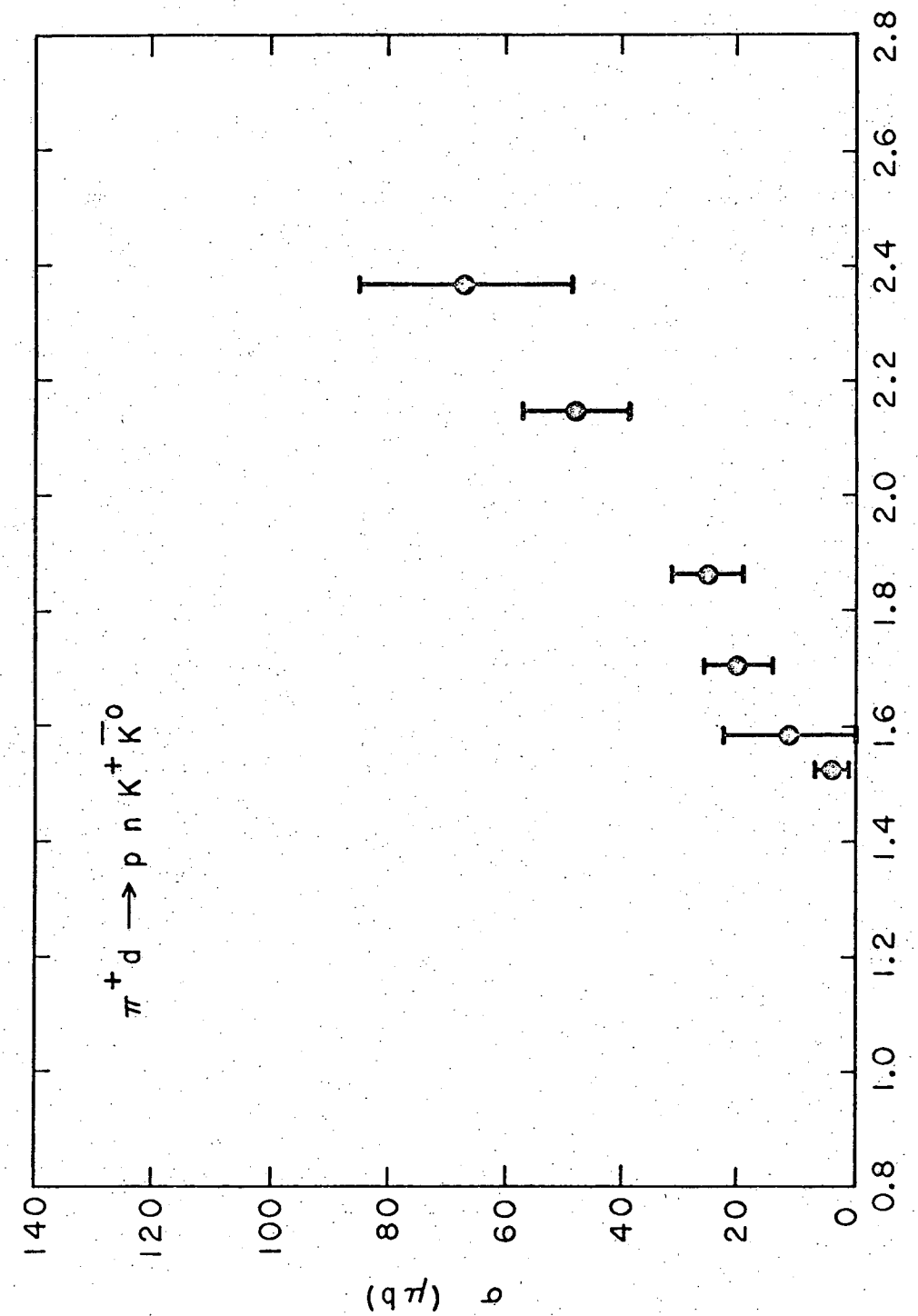

Fig. 14 Total cross section as a function of incident momentum for $pnK^+\bar{K}^0$ final state.

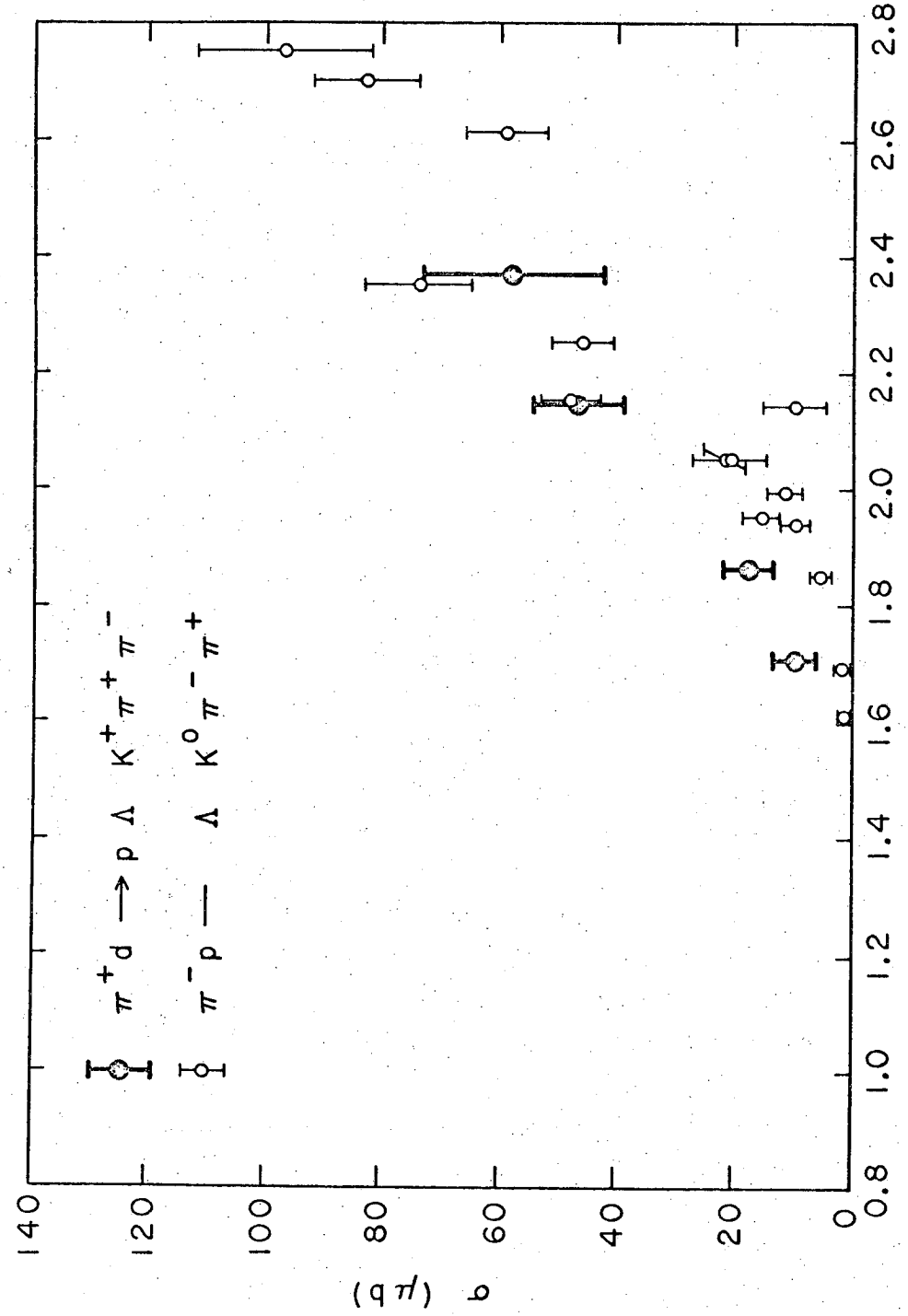

Fig. 15 Total cross section as a function of incident momentum for $p\Lambda K^+\pi^+\pi^-$ final state from this experiment (filled points), and $\Lambda K^0{}_-\pi^+$ final state from Refs. 1 and 2 and papers quoted therein (open points).

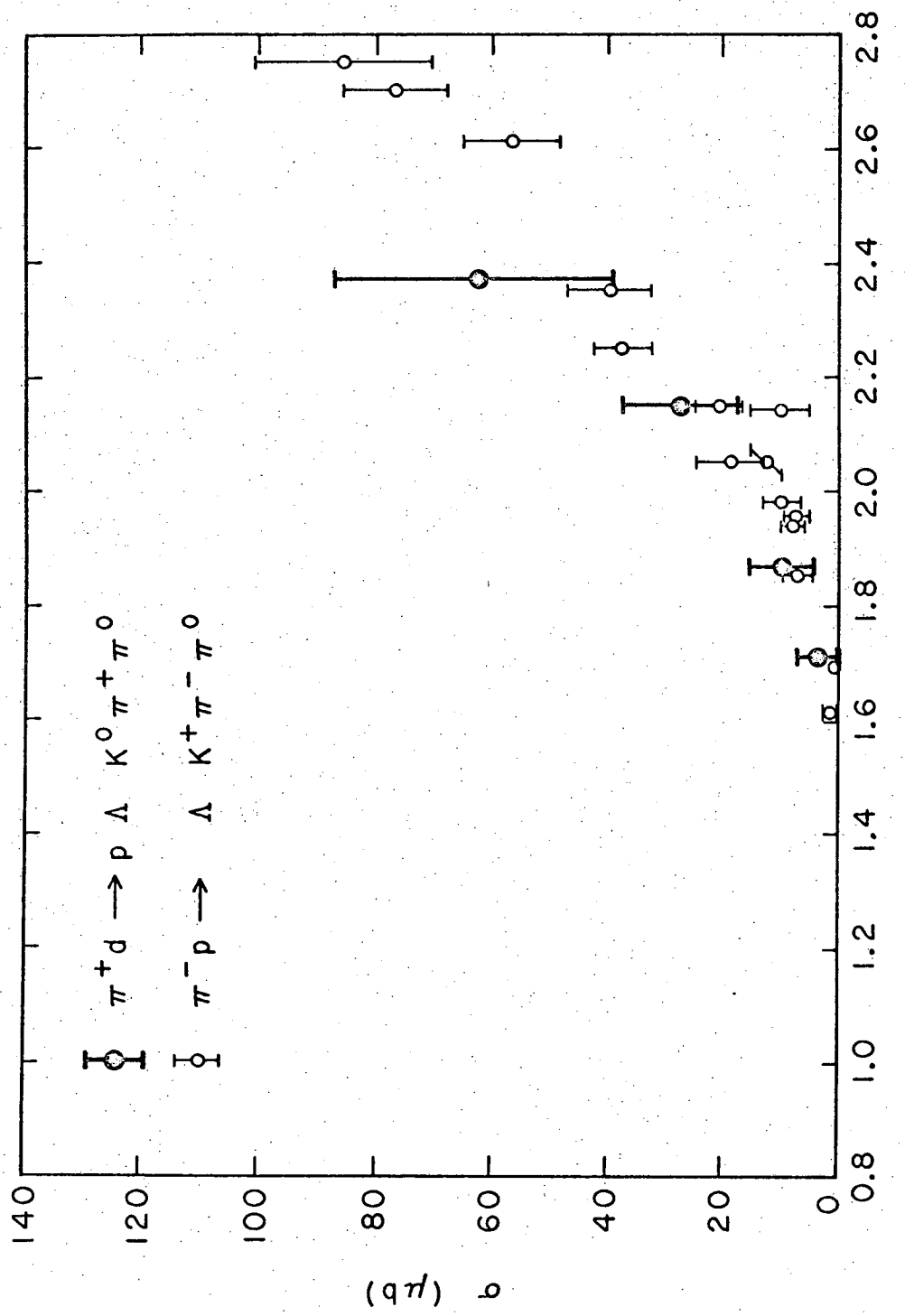

Fig. 16 Total cross section as a function of incident momentum for $p\Lambda K^o \pi^+ \pi^o$ final state from this experiment (filled points), and $\Lambda K^+ \pi^- \pi^o$ final state from Refs. 1 and 2 and papers quoted therein (open points).

If we assume that the reactions we observe can be explained in terms of the π interacting with one of the nucleons, we can compare the deuterium cross section with the corresponding πN cross section.[1,2,8,9] For $\pi^+ n$ reactions (final state with a proton) we have plotted the charge-symetric $\pi^- p$ cross section; for $\pi^+ p$ reactions (final states with a neutron) we have plotted the $\pi^+ p$ cross sections. These πN cross sections have been plotted with the πd cross sections in figs. 4-11 and figs. 15-16. The $\pi^+ d$ cross sections at a particular momentum should be an average of the πN cross section over ~ 0.2 GeV/c centered at the same momentum. In all cases where this comparison is possible the πd and πN cross sections compare well.

B. $\pi^+ p \longrightarrow \Lambda K^+ \pi^+$

We can use the $n\Lambda K^+ \pi^+$ final state to get information on the reaction

$$\pi^+ p \longrightarrow \Lambda K^+ \pi^+ .$$

Assuming the impulse model, the reaction $\pi^+ d \longrightarrow n\Lambda K^+ \pi^+$ can be thought of as

$$\begin{array}{l} \pi^+ p \longrightarrow \Lambda K^+ \pi^+ \\ (n) \longrightarrow (n) \end{array}$$

where the neutron is a spectator. As a check on the assumptions of the spectator model we can compare the neutron laboratory momentum

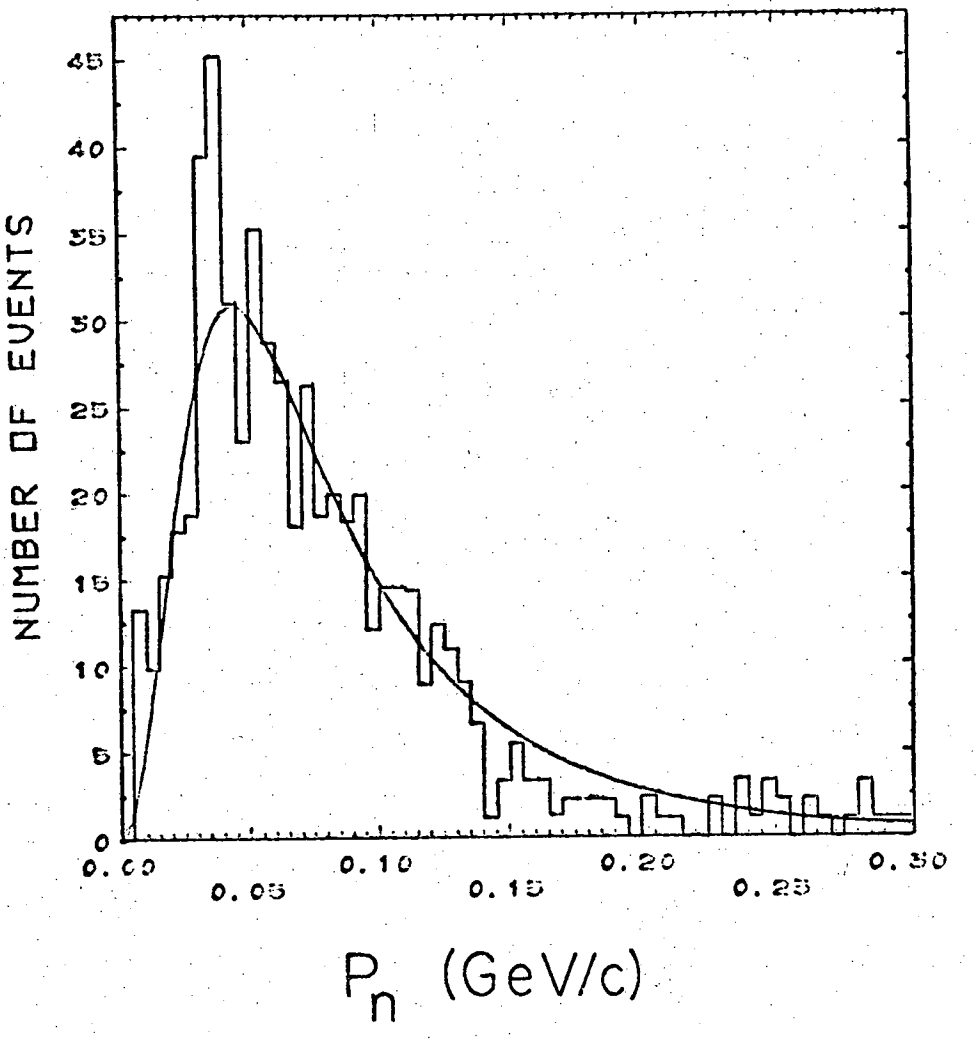

Fig. 17 Laboratory momentum distribution of neutrons from $n\Lambda K^+\pi^+$ final state. The curve is the prediction of the Hulthen wave function.

distribution to the prediction of one of the deuteron wave-functions; this is shown in fig.17 for events with a best fit to $n\Lambda K^+\pi^+$. In the rest of this analysis we have thrown out events with neutron momentum above 300 MeV/c and assumed that the impulse model was valid for the rest (85 $^o/_o$ of the total with best fits to this state). In order to reduce contamination from the $(n\gamma)$ $\Lambda K^+\pi^+$ final state the missing mass was required to be $0.82\ (GeV/c^2)^2 \leq mm^2 \leq 0.98\ (GeV/c^2)^2$. Dividing the remaining data into four c.m. energy intervals, we get the $\Lambda K^+\pi^+$ Dalitz plots and mass projections shown in figs.18 and 19. A maximum-likelihood fit was made to the amount, mass, and width of the $Y^*(1385)$ assuming a p-wave Breit-Wigner. The results are given in table III. Monte-Carlo events were generated at the mean c.m. energy for each interval and the results plotted over the mass projections in figs. 18 and 19.

The production angular distributions for events with $1.80\ (GeV/c^2)^2 \leq M_{\Lambda\pi}{}^2 \leq 2.02\ (GeV/c^2)^2$ are given in fig.20 after subtracting the appropriate amount of isotropic background. The production angle is defined as

$$\cos(\theta) = \frac{\vec{P}_{Y^*} \cdot \vec{P}_T}{|\vec{P}_{Y^*}|\,|\vec{P}_T|}$$

in the c.m. of the Y^*K system. $\vec{P}_T$ is the momentum vector of the target nucleon, defined here as

$$\vec{P}_T = \vec{P}_{deuteron} - \vec{P}_{neutron}.$$

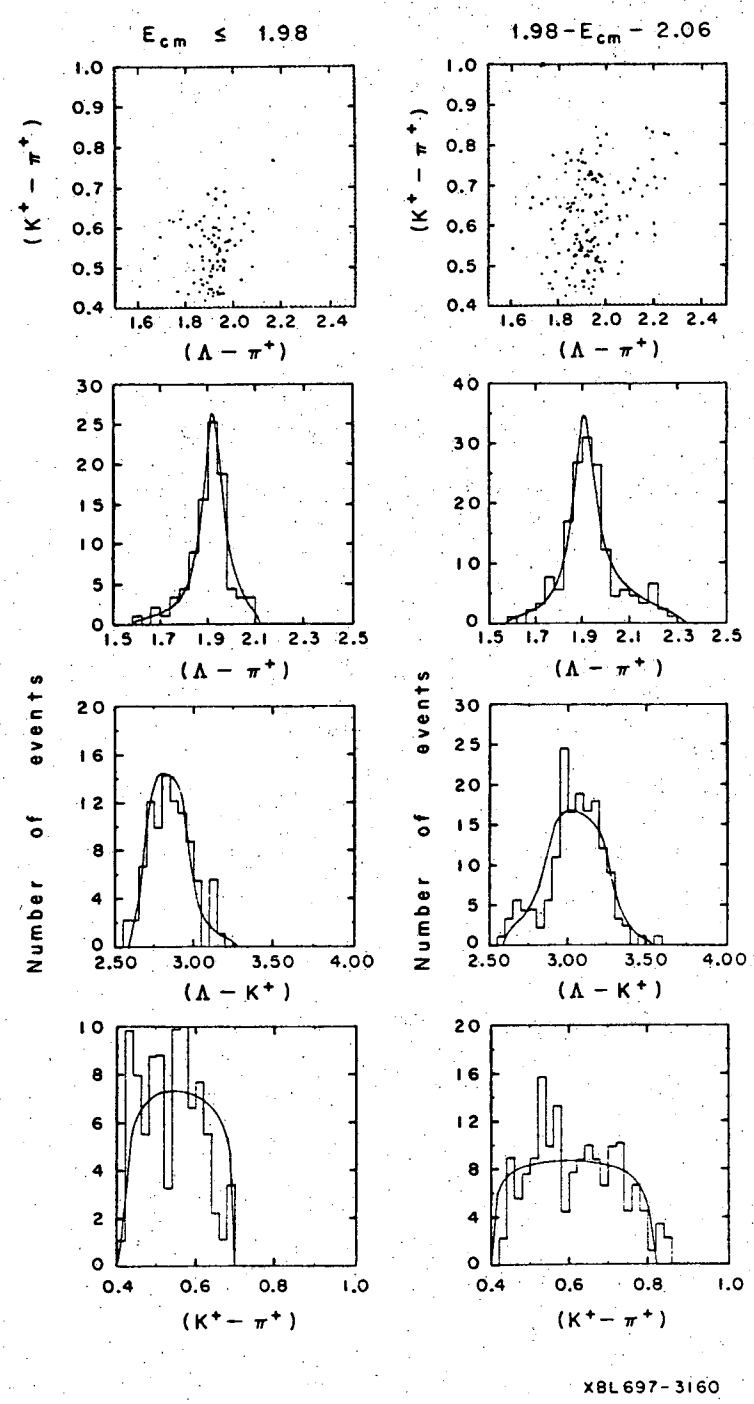

Fig. 18 Dalitz plots and effective mass squared projections for $\Lambda K^+\pi^+$ from $n\Lambda K^+\pi^+$ final state. Center of mass energy less than 1.98 GeV and 1.98 GeV - 2.06 GeV.

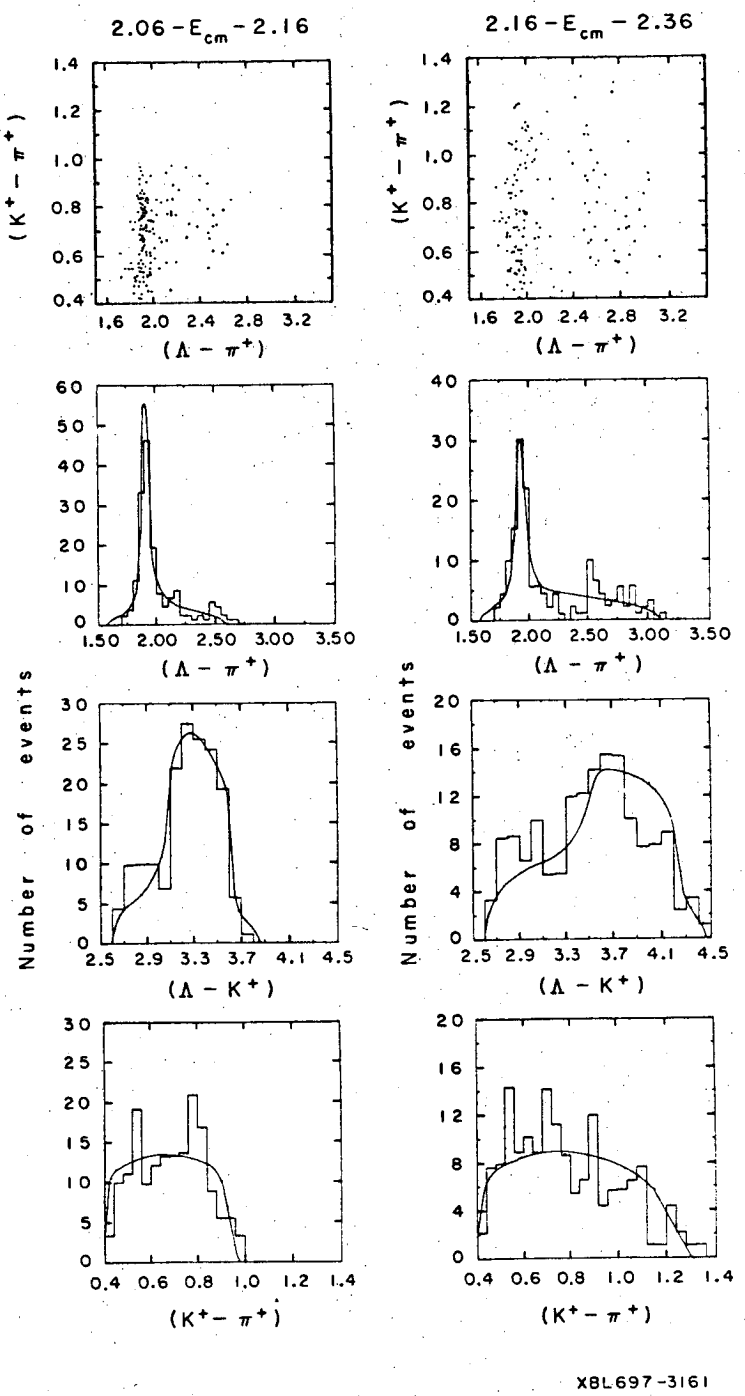

Fig. 19 Dalitz plots and effective mass squared projections for $\Lambda K^+\pi^+$ from $n\Lambda K^+\pi^+$ final state. Center of mass energy 2.06 GeV - 2.16 GeV and 2.16 GeV - 2.36 GeV.

Table III. $Y^*(1385)$ amount, mass, and width.

Center of mass energy (GeV)	Amount	Mass (GeV/c^2)	Width (GeV/c^2)
threshold - 1.98	0.92±.08	1.3866±.0044	0.049 ±.011
1.98 - 2.06	0.80±.09	1.3850±.0031	0.045 ±.010
2.06 - 2.16	0.69±.07	1.3828±.0020	0.0255±.0046
2.16 - 2.36	0.39±.06	1.3868±.0020	0.0217±.0062

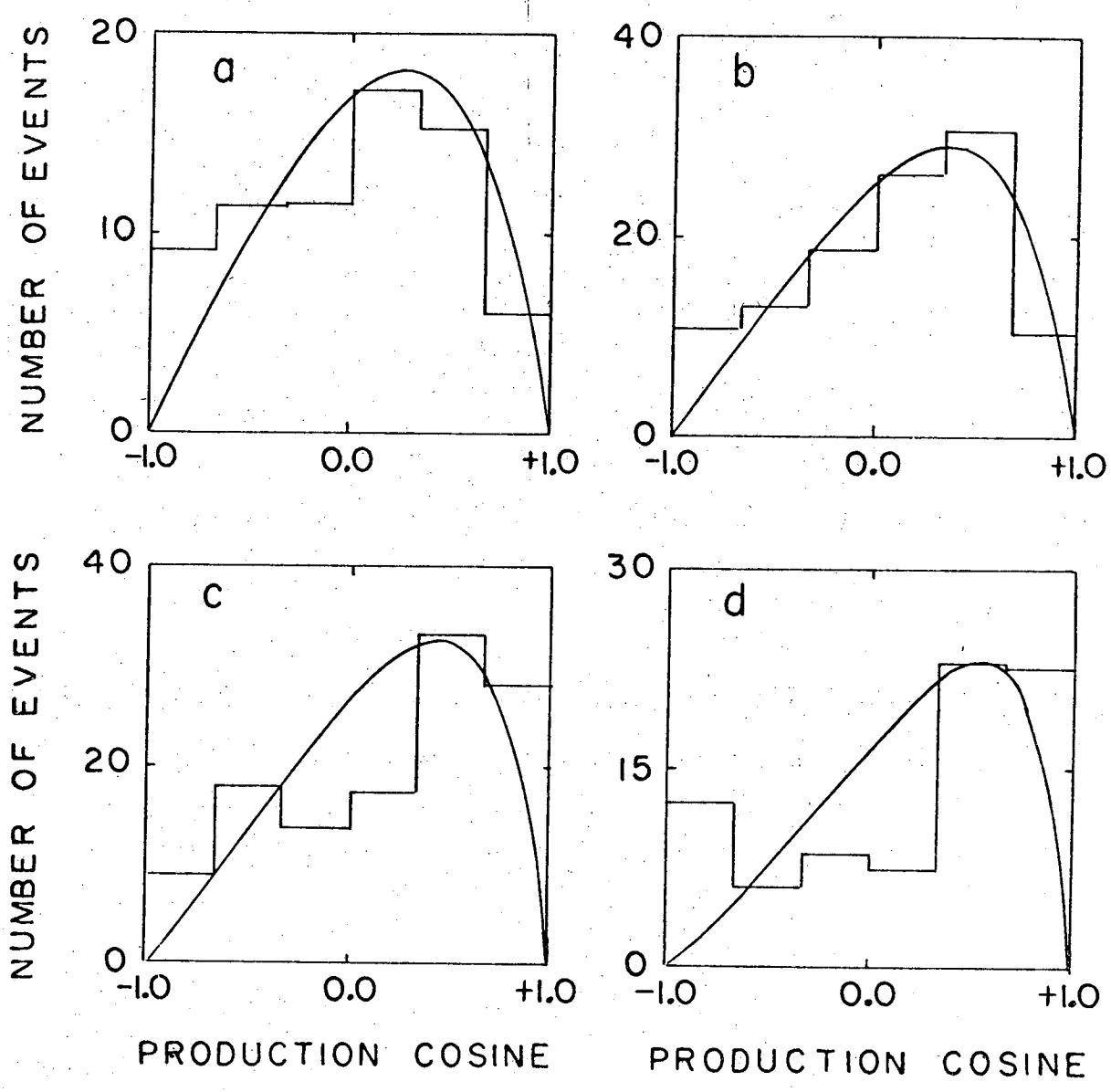

Fig. 20 Production angular distribution for $Y^*(1385)$ in reaction $\pi^+ p \rightarrow Y^* K$. Angle plotted is between the Y^* and the target proton in the $Y^* K$ center of mass. a) $E_{cm} < 1.98$, b) $1.98 < E_{cm} < 2.06$, c) $2.06 < E_{cm} < 2.16$, d) $2.16 < E_{cm} < 2.36$. Curves are predictions of ρ-photon analogy of Stodolski and Sakurai.

If we look for an explanation of the production distribution in terms of an s-channel description, we find that although there are many reported[10] $T=3/2$ πN resonances in this mass region, (2.0 GeV/c^2) none of them alone correctly reproduces the behaviour of the production distribution.

The lowest mass particle with the correct quantum numbers for exchange in the t-channel is the $K^*(890)$. In general the amplitude for this process is made up of three independent parts (corresponding to the three ways of coupling the $\frac{1}{2}^+$ nucleon, the 1^- K^* and some relative orbital angular momentum to make the $3/2^+$ Y^*). However, there is a model that makes a specific prediction, the so-called ρ-photon analogy of Stodolski and Sakurai.[11,12] For a description of the model see Appendix B.

The ρ-photon analogy prediction for the differential cross section is

$$\frac{d\sigma}{d\Omega} \propto \frac{\sin^2\theta}{(t - m_{K^*}^2)^2}$$

where t is the square of the four-momentum transfer $(p_\pi - p_K)^2$. This is the function plotted over the production distributions in fig. 20 (a-d). The fit is good at the lower two energies, poor at the higher ones. The failure of the model at higher energies is not unexpected, however - simple exchange models without absorption have always failed to give the correct amount of forward peaking in production distributions at higher energies. There is also the possibility of baryon exchange (Λ or Σ^0 for example) playing a small role and giving a back-

ward peak to the production distribution, as is indeed the case at slightly higher momentum.[13]

The model also makes predictions about the decay distribution of the Y^*; these are most conveniently expressed in terms of the Y^* spin density matrix elements. In the rest system of the Y^* we take the z-axis parallel to the incoming target proton and the y-axis is the normal to the production plane. In terms of fig.21

$$\hat{n} = \frac{\vec{p}_K \times \vec{p}_p}{|\vec{p}_K||\vec{p}_p|} .$$

With this choice of coordinate system, the density matrix elements for the Y^* are given in table IV and fig. 22 for the four c.m. energy intervals. The ρ-photon analogy predictions are $\rho_{33} = 3/8$, $Re(\rho_{31}) = 0$, $Re(\rho_{3-1}) = \sqrt{3}/8$; these are the straight lines plotted on fig. 22.

Near threshold the Stodolski-Sakurai ρ-photon analogy fits our data very well; this is similar to what is seen in the reaction $K^+p \rightarrow \Delta^{++}K^o$ near threshold[14] and the reaction $\pi^+p \rightarrow \Delta^{++}\pi^o$ at moderate energies[15], reactions to which the model is also applicable. Above 2.06 GeV this model fails to explain our data.

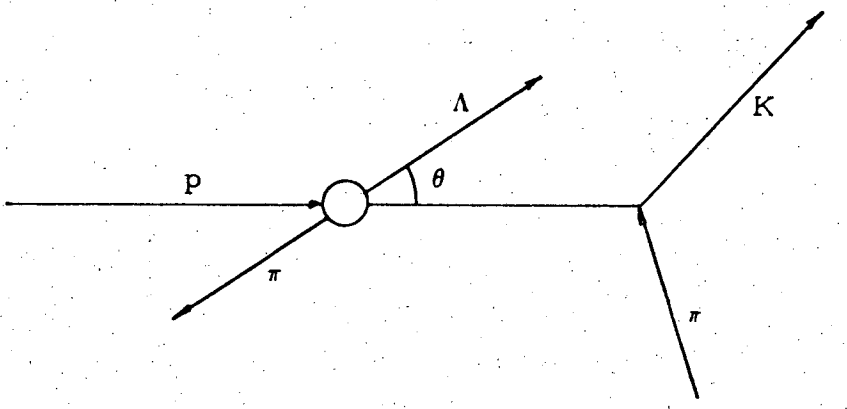

Fig. 21 Coordinate system used for Y^* decay distributions. $\hat{z}$:incoming nucleon direction; $\hat{y}$:normal to production plane; $\hat{x}$:$\hat{y}\times\hat{z}$

Table IV. Y^* density matrix elements in $\pi^+ p \rightarrow Y^{*+} K^+$.

Center of mass energy (GeV)	$\rho_{3,3}$	$Re(\rho_{31})$	ρ_{3-1}
threshold - 1.98	0.39±.05	0.07±.05	0.17±.07
1.98 - 2.06	0.42±.05	0.02±.06	0.27±.06
2.06 - 2.16	0.12±.06	0.07±.06	0.24±.06
2.16 - 2.36	0.21±.06	-0.05±.07	0.18±.07

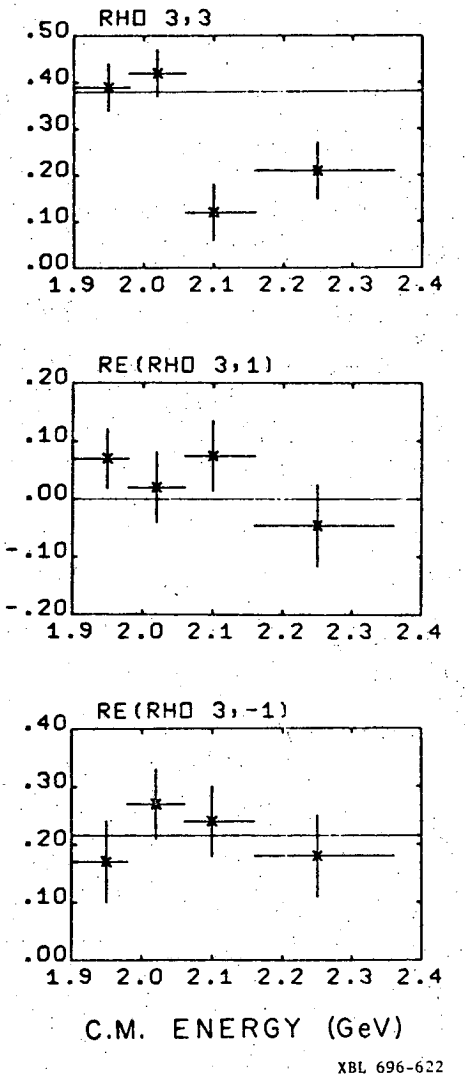

Fig. 22 Y^* density matrix elements. Straight lines are predictions of ρ-photon analogy.

C. $\pi^+ p \longrightarrow \Sigma^+ K^o \pi^+$

The $n\Sigma^+ K^o \pi^+$ final state allows us to analyze the reaction

$$\pi^+ p \longrightarrow \Sigma^+ K^o \pi^+$$

Fig.23 shows the $\Sigma K\pi$ Dalitz plot and mass projections for all events with a best fit to $n\Sigma^+ K^o \pi^+$. Note the very conspicuous $K^*(890)$. Fig.24 shows the $\Sigma K\pi$ center of mass energy for all events. Although the threshold energy for $\Sigma K\pi$ is 1.82 GeV there are no events until the energy is sufficient to make a K^* (around 2.05 GeV). Table V gives the amount, mass, and width of the K^* in this final state. The curves plotted over the mass projections in fig.23 were obtained from Monte Carlo events generated with the K^* parameters given in table V and the center of mass energy distribution shown in fig. 24.

The center of mass production distribution for K^* events $(0.72\ (\text{Gev}/c^2)^2 \leq m^2_{K\pi} \leq 0.86\ (\text{GeV}/c^2)^2)$ is given in fig.25(a). All the angular distributions have been corrected for the small amount of background present in this $K\pi$ mass interval. Within the limited statistics of the data the production distribution is consistent with isotropy.

The K^* decay distributions are shown in fig. 25 (b, c) and the density matrix elements given in table VI . The curves plotted over the data in fig. 25 (b, c) correspond to the density matrix elements of table VI .

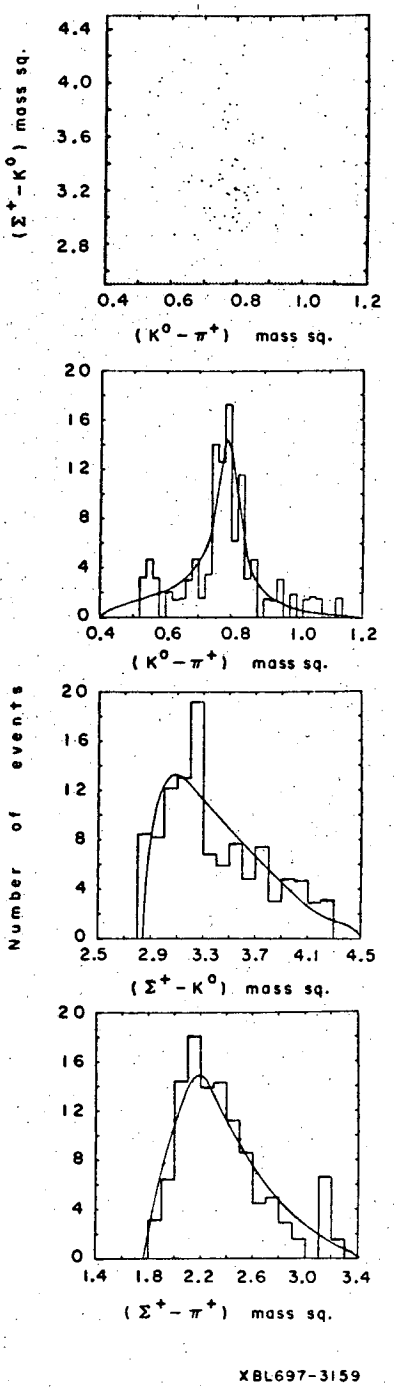

Fig. 23 Dalitz plot and effective mass squared for $\Sigma^+ K^0 \pi^+$ from $n\Sigma^+ K^0 \pi^+$ final state.

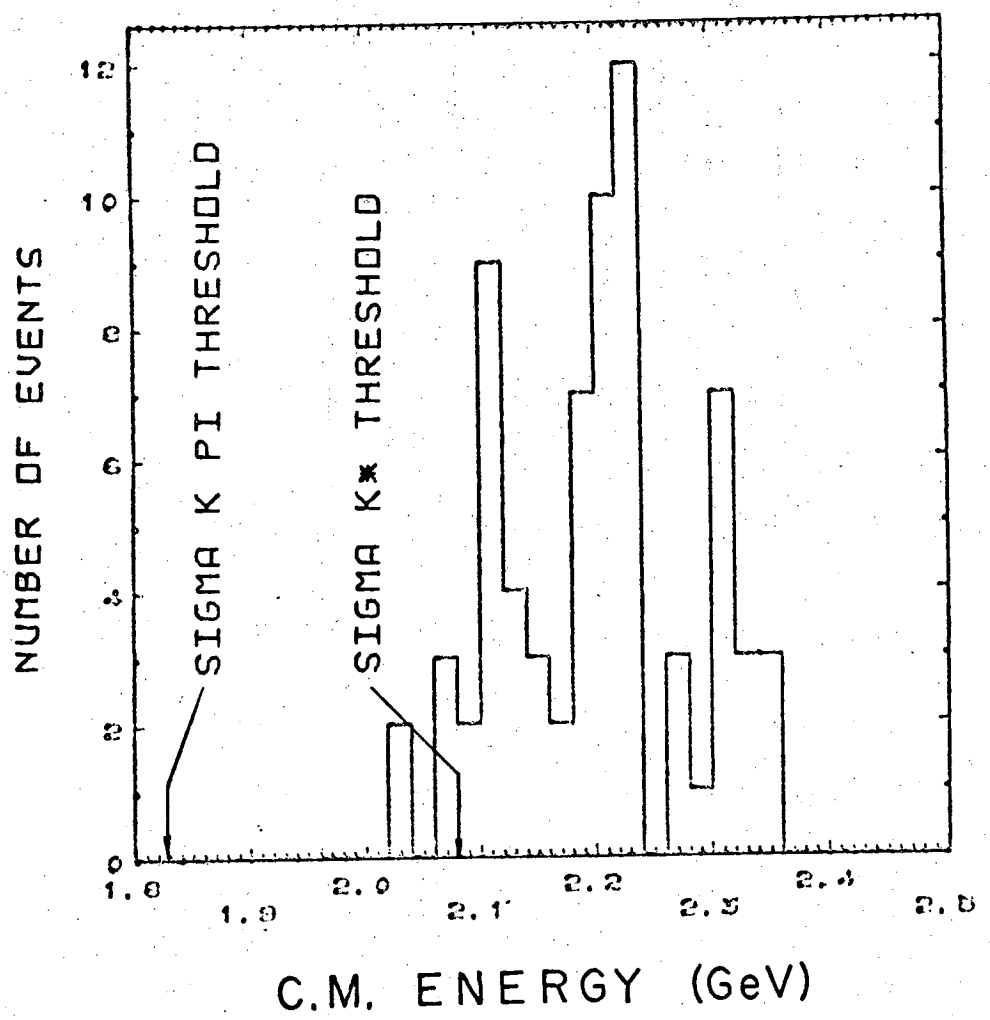

Fig. 24 Center of mass energy for $\Sigma^+K^0\pi^+$ from $n\Sigma^+K^0\pi^+$ final state.

Table V. $K^*(890)$ parameters in $\pi^+ p \rightarrow \Sigma^+ K^{*+}$.

Amount	Mass (GeV/c^2)	Width (GeV/c^2)
0.75±.10	0.895±.006	0.051±.017

Table VI. $K^*(890)$ density matrix elements in $\pi^+ p \rightarrow \Sigma^+ K^{*+}$.

$\rho_{0,0}$	$\rho_{1,1}$	$\rho_{1,-1}$	$Re(\rho_{1,0})$
0.124±.082	0.438±.041	0.063±.074	0.097±.050

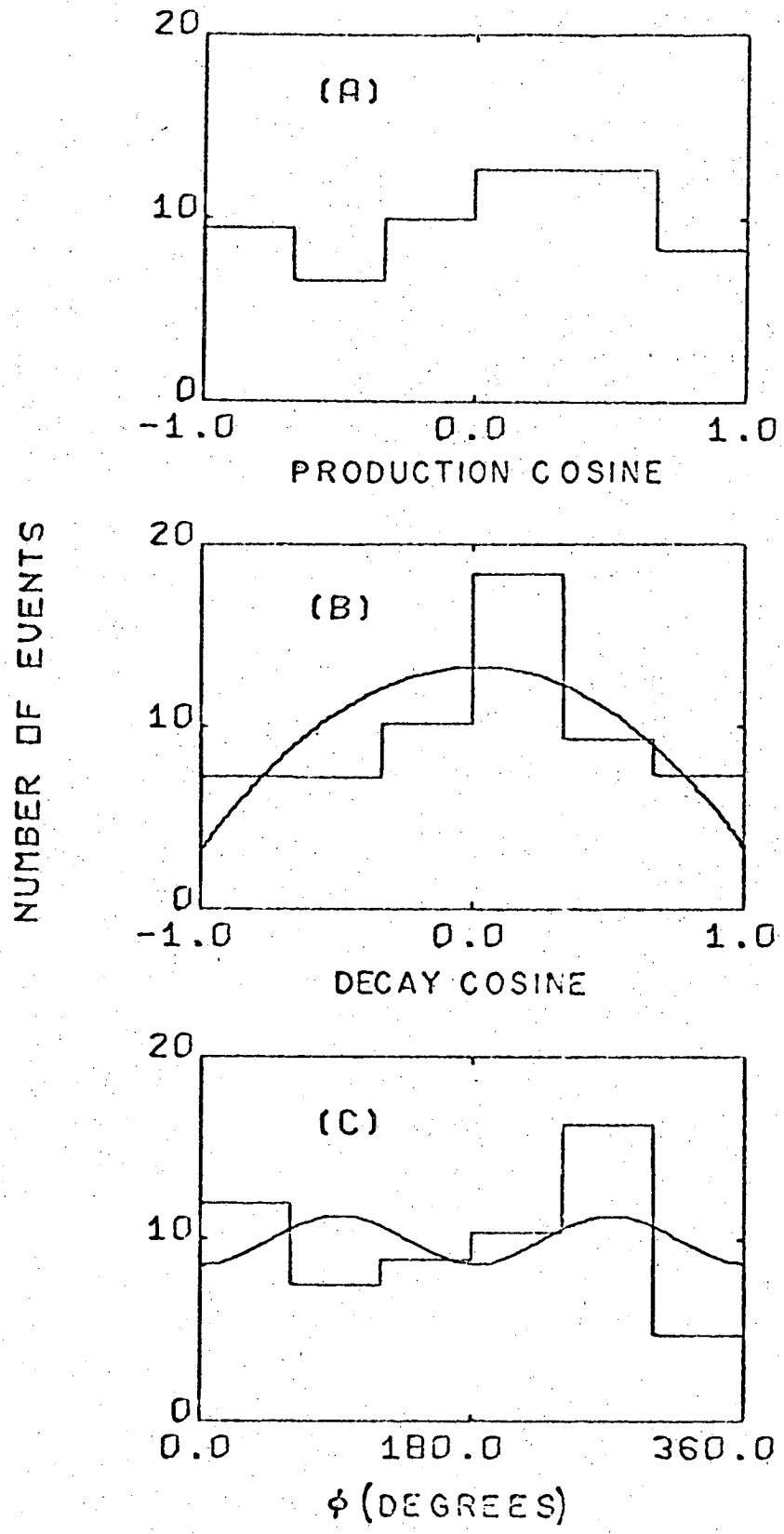

Fig. 25 $K^*(890)$ production and decay distributions. a) production cosine. b) decay cosine. c) Treiman-Yang angle. The curves correspond to the density matrix elements of table VI.

D. $\pi^+ n \longrightarrow pK^+K^-$

As well as the obvious strange particle events with vees we were also able to obtain the ppK^+K^- final state. As another part of the experiment, all of the 4-prong events have been measured and processed; besides the non-strange-particle final states possible for this topology we also attempted to fit ppK^+K^-. Although the expected number of these events was only a very small fraction of the total of that topology ($\sim .1\ ^{o}/_{o}$), if both protons have enough momentum to be visible the ppK^+K^- final state is a 4-constraint fit and very hard for other final states to fake. Furthermore the measuring of all of these events was done on the Spiral Reader which puts out track ionization information. Requiring the event to have a good kinematic fit to ppK^+K^- and also to have a low ionization χ^2 to this hypothesis resulted in approximately 250 ppK^+K^- candidates. These events were all looked at on the scanning table and events which were not ppK^+K^- were deleted. The end result was 150 4-constraint events with negligible contamination.

Defining the spectator nucleon as the proton with the lower laboratory momentum, and making a cut on spectator momentum at 300 MeV/c results in the c.m. energy distribution shown in fig. 26 . Here the c.m. energy is defined as the energy in the pK^+K^- system, where p is the non-spectator proton.

By comparing this c.m. energy distribution to a reaction with a known cross section, the $\pi^+ n \rightarrow pK^+K^-$ cross section can be determined as described in Appendix A. In this case the reactions that were used

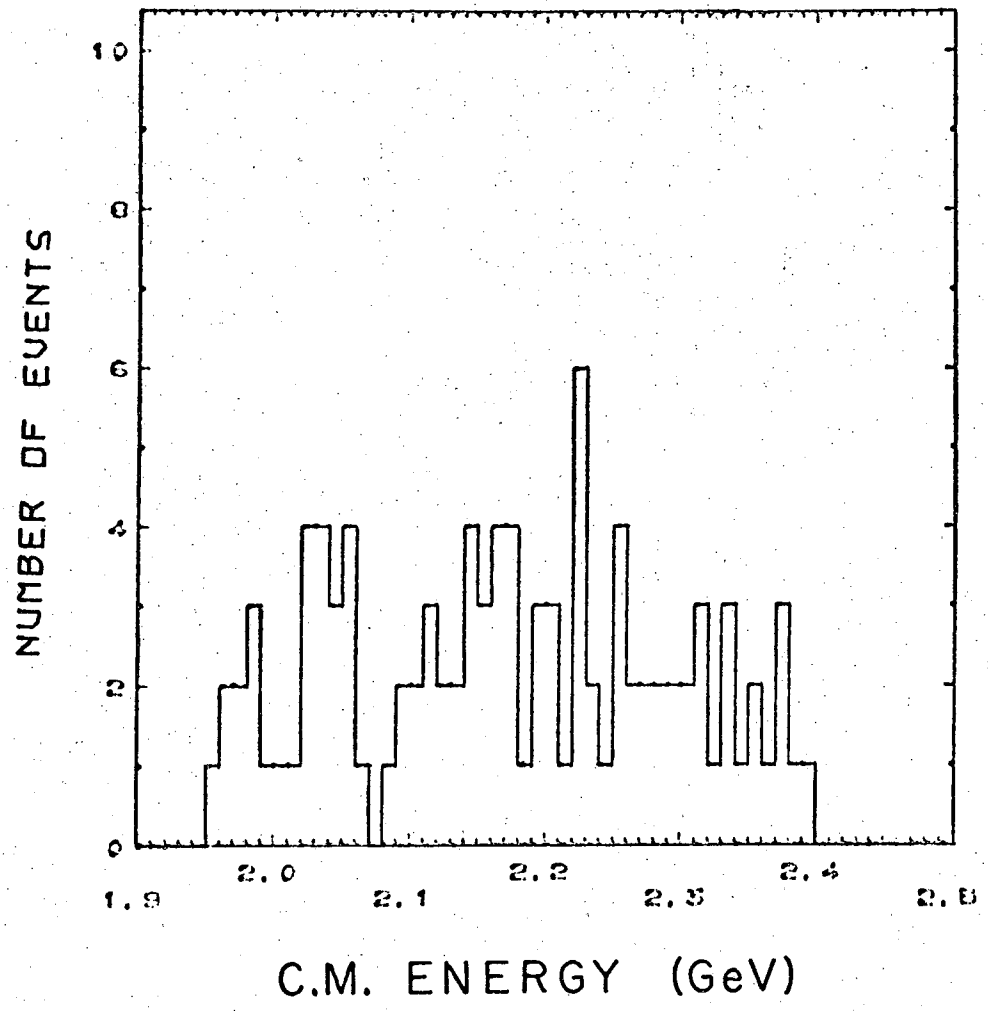

Fig. 26 Center of mass energy for pK^+K^- from ppK^+K^- final state.

were

$$\pi^+ n \longrightarrow p\pi^+\pi^-$$
$$p\pi^+\pi^-\gamma$$
$$p\pi^+\pi^-\pi^o$$
$$p\pi^+\pi^-(\text{missing mass}).$$

The sum of these four reactions should, by charge symmetry, have the same cross section as

$$\pi^- p \longrightarrow n\pi^+\pi^-$$
$$\pi^+\pi^-(\text{missing mass}).$$

The cross section for the sum of these two reactions is known[6] and allows us to determine the pK^+K^- cross section. Dividing the c.m. energy distribution into three intervals we get the cross sections given in table VII and fig. 27.

The pK^+K^- Dalitz plots and mass squared projections for these three c.m. energy intervals are given in fig. 28. The $\phi(1020)$ is evident in the K^+K^- mass spectrum in intervals 1 and 3; there is also indication of $\Lambda(1520)$ production in the pK^- mass spectrum of interval 2. Due to the small number of events it was impossible to do a fit to the amount of ϕ and $\Lambda(1520)$ in each interval; instead the number of events above background was estimated. Monte-Carlo events were generated with this estimate of the amount of resonance and plotted as the curve over the data in fig. 28. The estimated amounts are given in table VIII.

Table IX gives the cross section for production of ϕ and $\Lambda(1520)$. Fig. 29(a) shows the production distribution for ϕ events ($1.02\ (\text{GeV}/c^2)^2 < m^2_{K^+K^-} < 1.06\ (\text{GeV}/c^2)^2$) and fig. 29(b,c) shows the decay distributions.

Table VII. Cross section for $\pi^+ n \rightarrow p K^+ K^-$

Center of mass energy (GeV)		Cross section (μb)
E1:	1.95 - 2.10	38±7
E2:	2.10 - 2.25	67±10
E3:	2.25 - 2.40	102±19

Table VIII. Fraction of $\phi(1020)$ and $\Lambda(1520)$

Center of mass energy (GeV)		Estimated fraction ϕ	Λ
E1:	1.95 - 2.10	0.5	0.0
E2:	2.10 - 2.25	0.1	0.3
E3:	2.25 - 2.40	0.2	0.1

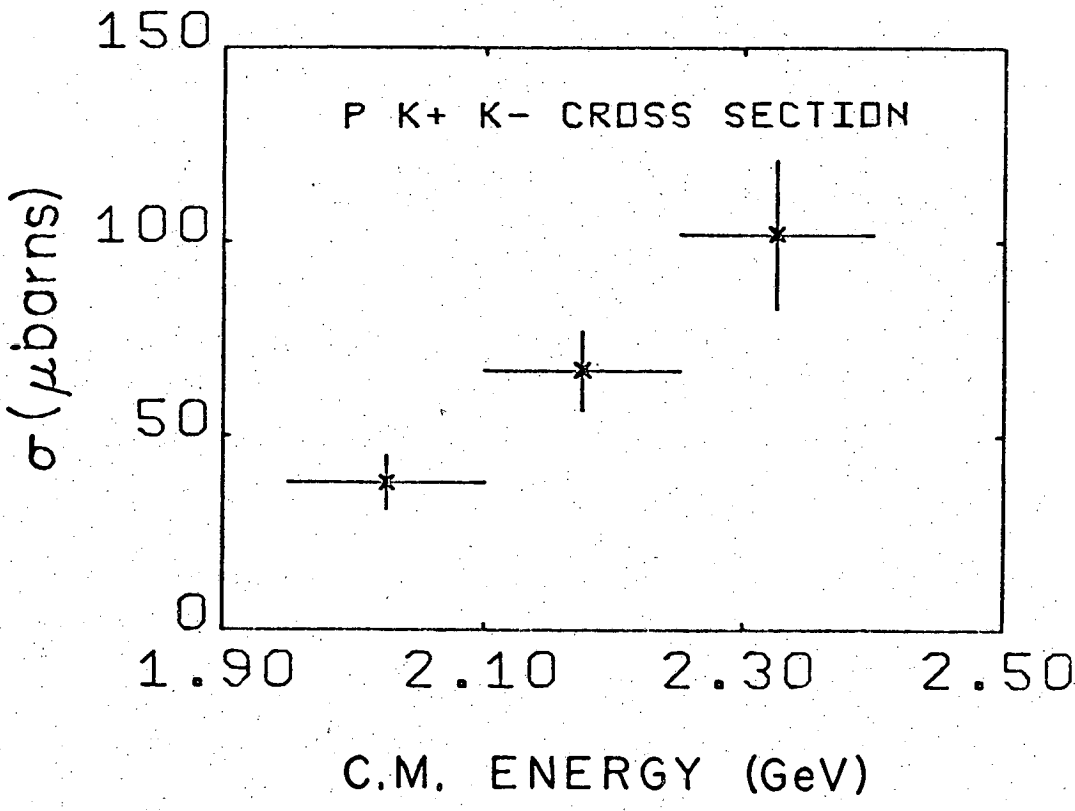

Fig. 27 Total cross section for pK^+K^- as a function of center of mass energy.

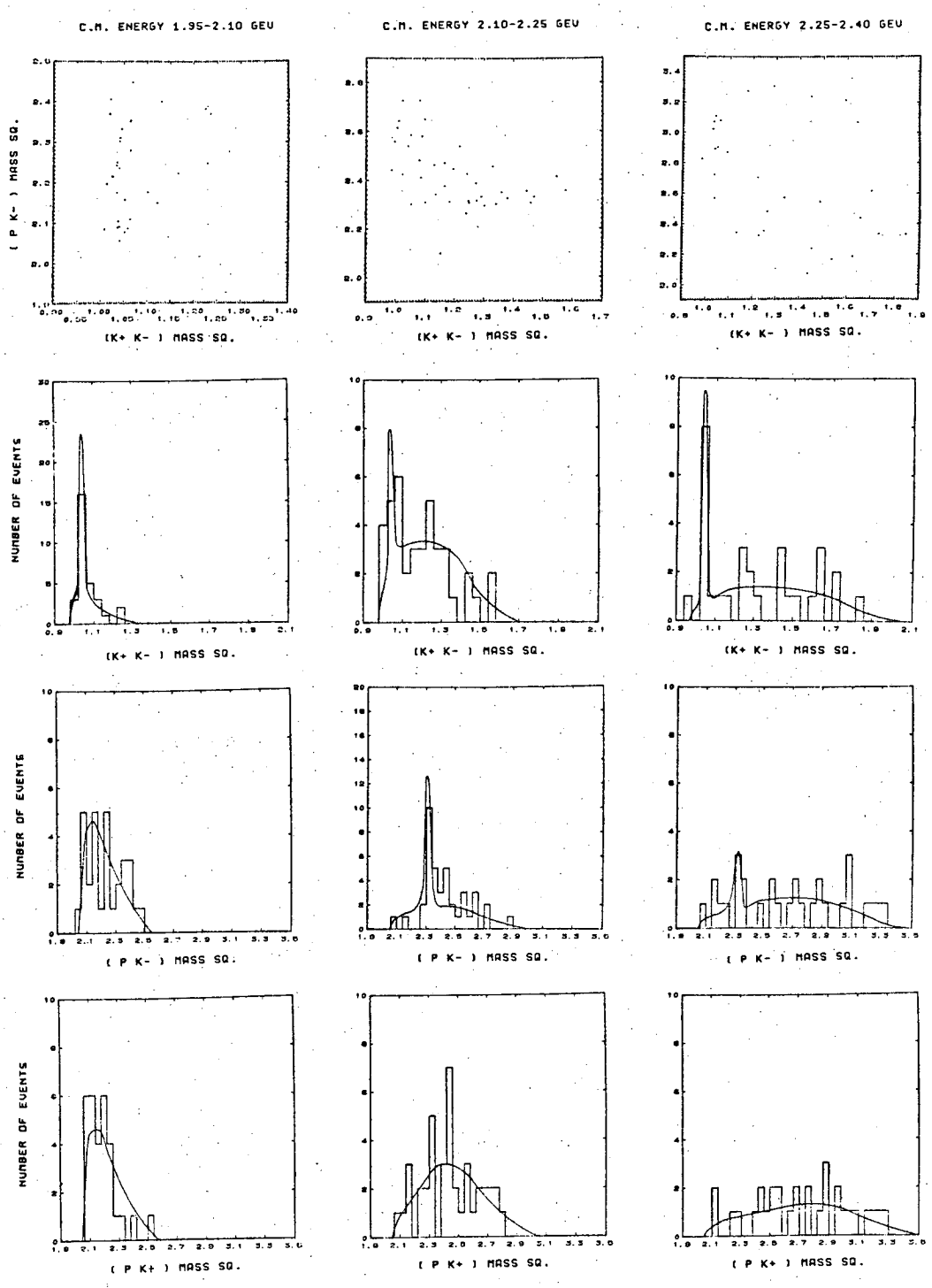

Fig. 28 Dalitz plots and effective mass squared projections for pK^+K^- from ppK^+K^- final state. Center of mass energy intervals 1.95 GeV - 2.10 GeV, 2.10 GeV - 2.25 GeV, and 2.25 GeV - 2.40 GeV.

Table IX. Cross sections for $\pi^+ n \rightarrow p\phi$ and $\pi^+ n \rightarrow \Lambda(1520)K^+$.

	Center of mass energy (GeV)	Cross section (μbarns) $\pi^+ n \rightarrow p\phi$	Cross section (μbarns) $\pi^+ n \rightarrow \Lambda(1520)K^+$
E1	1.95 - 2.10	38 ± 11	0 ± 13
E2	2.10 - 2.25	$14 \,^{+\,21}_{-\,6}$	94 ± 36
E3	2.25 - 2.40	42 ± 17	$45 \,^{+\,45}_{-\,31}$

Table X. Density matrix elements for $\phi(1020)$.

$\rho_{0,0}$	$\rho_{1,1}$	$\rho_{1,-1}$	$Re(\rho_{1,0})$
0.64±.14	0.18±.07	-0.24±.09	-0.25±.08

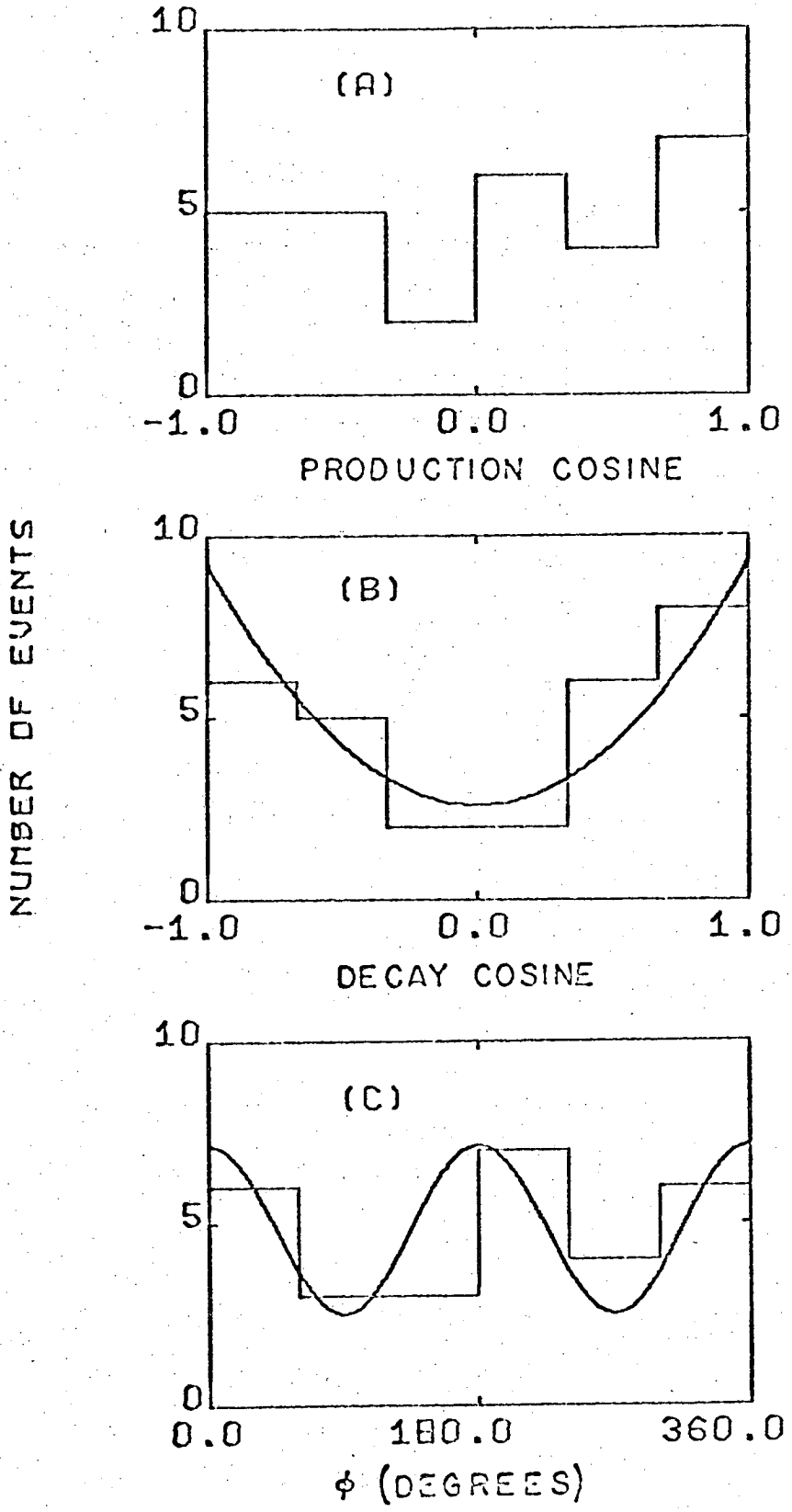

Fig. 29 Production and decay distributions for $\phi(1020)$. a) production cosine. b) decay cosine. c) Treiman-Yang angle. The curves plotted over b) and c) correspond to the density matrix elements of table X.

Table X contains the ϕ density matrix elements. The production is consistent with an isotropic distribution; even with the limited numbers of events available, however, it is clear from the decay distribution that the ϕ is produced highly aligned. The curves plotted over fig. 29(b,c) correspond to the density matrix elements of table X. If the ϕ was produced by ρ-exchange it would be highly aligned; however simple ρ-exchange without absorption predicts a decay distribution of the form $\sin^2\theta$, completely different from the observed distribution. This failure of a simple ρ-exchange model is very similar to the situation seen in ω production [16] (same quantum numbers as the ϕ) where the density matrix elements are very similar to those of table X.

IV. SUMMARY AND CONCLUSIONS

Cross sections for production of strange particles by π mesons on deuterium have been presented. Three final states have been analyzed in terms of the impulse model to obtain information on πN reactions.

$Y^*(1385)$ production dominates the reaction $\pi^+ p \rightarrow \Lambda K^+ \pi^+$ and the production of this isobar is well described by M1 K^* exchange near threshold, but not at higher energies.

The reaction $\pi^+ p \rightarrow \Sigma^+ K^o \pi^+$ is almost entirely $\pi^+ p \rightarrow \Sigma^+ K^{*+}$ at the energies of this experiment.

Highly aligned ϕ's are produced in the reaction $\pi^+ n \rightarrow p K^+ K^-$ along with $\Lambda(1520)$; simple ρ-exchange does not predict the correct alignment.

ACKNOWLEDGMENTS

This report is the end result of the work of many people: the Bevatron staff, the 72 inch bubble chamber crew, the scanning and measuring staff, the computer center staff, and others.

I am especially indebted to Wally Hendricks for his excellent handling of the scanning and measuring of the film.

It is a pleasure to acknowledge many useful discussions with Jerry Danburg, and the advice and encouragement of Profs. Donald Miller and Janos Kirz.

Finally, I am especially grateful to Prof. Luis Alvarez for his example, his hospitality, and his beer.

This work was done under the auspices of the U. S. Atomic Energy Commission.

APPENDICES

A. Extracting Single-nucleon Physics from Reactions on Deuterium

There are some reactions that cannot be analyzed in a bubble chamber because of the presence of two or more unseen particles in the final state. For example the reaction

$$\pi^- p \rightarrow n\omega, \ \omega \rightarrow \pi^+ \pi^- \pi^0$$

cannot be analyzed because one cannot measure the momentum vectors of either the neutron or the π^0.

If we assume that the interactions we are dealing with are independent of isotopic spin projection, however, there are other reactions which give us the same physics and perhaps are analyzable; in the example above the charge-symmetric reaction is

$$\pi^+ n \longrightarrow p\omega, \ \omega \longrightarrow \pi^+ \pi^- \pi^0;$$

now with only the π^0 missing the reaction is in fact over-determined -- four equations of constraint at the production vertex (3-momentum and energy) and only three unknown quantities, the π^0 3-momentum.

Free neutron targets are not available; however the deuteron with its low binding energy of 2.2 MeV provides a source of "almost free" neutrons. If the range of interaction and wavelength of the incoming beam are short compared to the separation between nucleons, the beam could interact with one nucleon instead of the whole deuteron, leaving the "spectator" nucleon behind with the momentum it had before the interaction. This is the impulse model. It is the basic assumption in using deuterons as a source of nucleon targets. To see how good it is and what its limitations are we would like to check its predictions against experimental distributions. The most straight-forward check is to look

at its predictions for the spectator nucleon.

The deuteron has been extensively studied and its wave function determined fairly well down to distances of the order of 0.1 fermi. Various popular wave functions tend to have the same behaviour over most of the deuteron volume, differing only at the core. See Ref. 17 for examples of the different wave functions. One of the most popular wave functions is the "Hulthen" wave function. Its properties are shown in fig. 30.

Looking at the momentum distribution we see that the nucleons have a mean momentum of about 60 MeV/c with significant probability all the way out to about 300 MeV/c. We are therefore dealing with a moving target. This Fermi motion causes a spread in the beam-nucleon center of mass energy for any particular beam momentum. Fig. 31 gives an illustration of this for 2.0 GeV/c π's on deuterium. Since the beam momentum in the πd reaction does not specify the energy of the πN state, it is customary to divide the data in terms of center of mass energy rather than beam momentum.

This model gives the distribution in momentum (fig. 30(b)) and angle (isotropic) for the nucleons in a deuteron. Even in the impulse approximation however these are not the distributions one would expect for the spectator nucleons in the laboratory. Two things modify this distribution:

i) Dependence of cross section on c.m. energy. For example if we have a 2 GeV/c π beam and threshold for the reaction of interest is at 2.1 GeV/c for a stationary nucleon, only reactions where the beam strikes a nucleon coming toward it will have sufficient

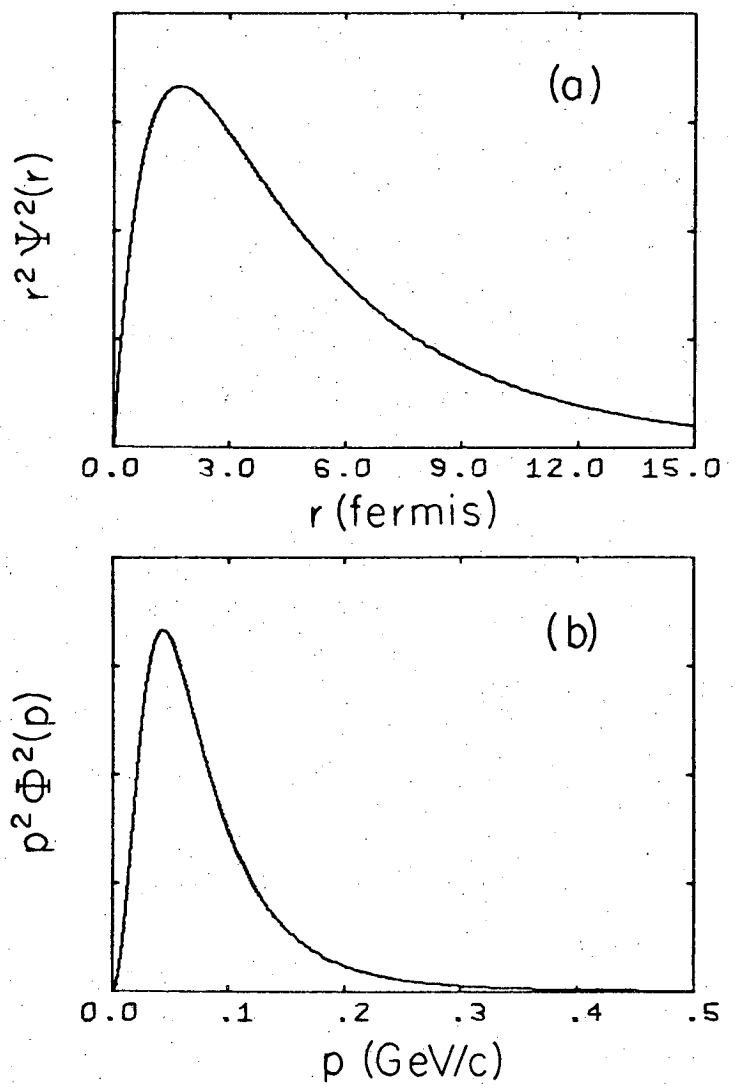

Fig. 30 a) Spatial distribution and b) momentum distribution from Hulthen wave function. Properties

Potential $\propto e^{-\beta r}/(e^{-\alpha r} - e^{-\beta r})$

Spatial wave function $\propto (e^{-\alpha r} - e^{-\beta r})/r$

Momentum wave function $\propto (p^2 + \alpha^2)^{-1} - (p^2 + \beta^2)^{-1}$

$\alpha = 0.232$ fe^{-1} $= 0.0457$ (GeV/c)$^{-1}$

$\beta = 1.202$ fe^{-1} $= 0.237$ (GeV/c)$^{-1}$

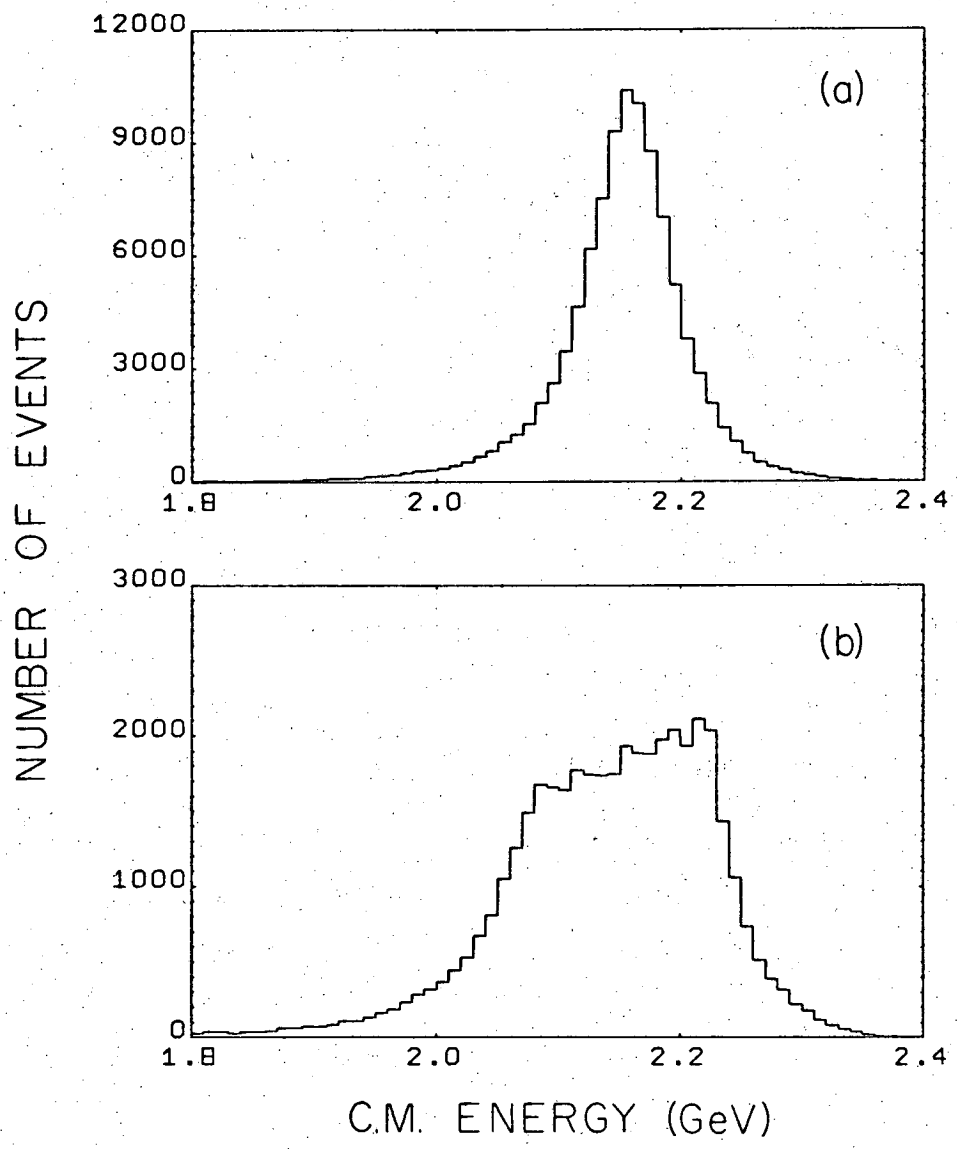

XBL 696-621

Fig. 31 Predictions of the impulse model for the center of mass energy distribution for 2.0 GeV/c π mesons on deuterium. (Monte-Carlo calculation) a) all spectator momentum b) spectator momentum greater than 80 MeV/c.

energy to be above threshold. Therefore all spectators, which have the opposite momentum to the target, will be of high momentum, and will be going forward with respect to the beam.

ii) Flux factor. Even with a constant cross section, the predicted angular distribution of spectators with respect to the beam is not isotropic. The number of reactions/unit time is proportional to the product of the flux and the cross section. The flux factor is given by

$$\left\{E_b^2 E_T^2 - (\vec{P}_b . \vec{P}_T)^2 - m_b^2 m_T^2\right\}^{\frac{1}{2}}$$

where E_b and E_T are the beam and target energies, $\vec{P}_b$ and $\vec{P}_T$ are their 3 - vector momenta, and m_b and m_T are their masses. This formula just expresses the fact that there are going to be more reactions per unit time when the targets are moving toward the beam than when they are moving away from it. This factor also causes the spectators to go preferentially in the forward direction, the effect being more pronounced the higher the spectator momentum. Fig. 32(a) shows the expected spectator angular distribution for all spectator momentum; fig. 32(b) is the distribution expected for events with spectators above 80 MeV/c (corresponding to the minimum momentum required for a proton to leave a visible track).

This is the impulse model prediction for the spectator nucleon momentum.

Although it is a reasonably good approximation to reality it suffers from one obvious defect when compared to experiment. If one plots the laboratory momentum distribution of the spectator nucleon for a reaction with a sensibly constant cross section and compares it with the predictions of the model, good agreement is found to 250-300 MeV/c, but

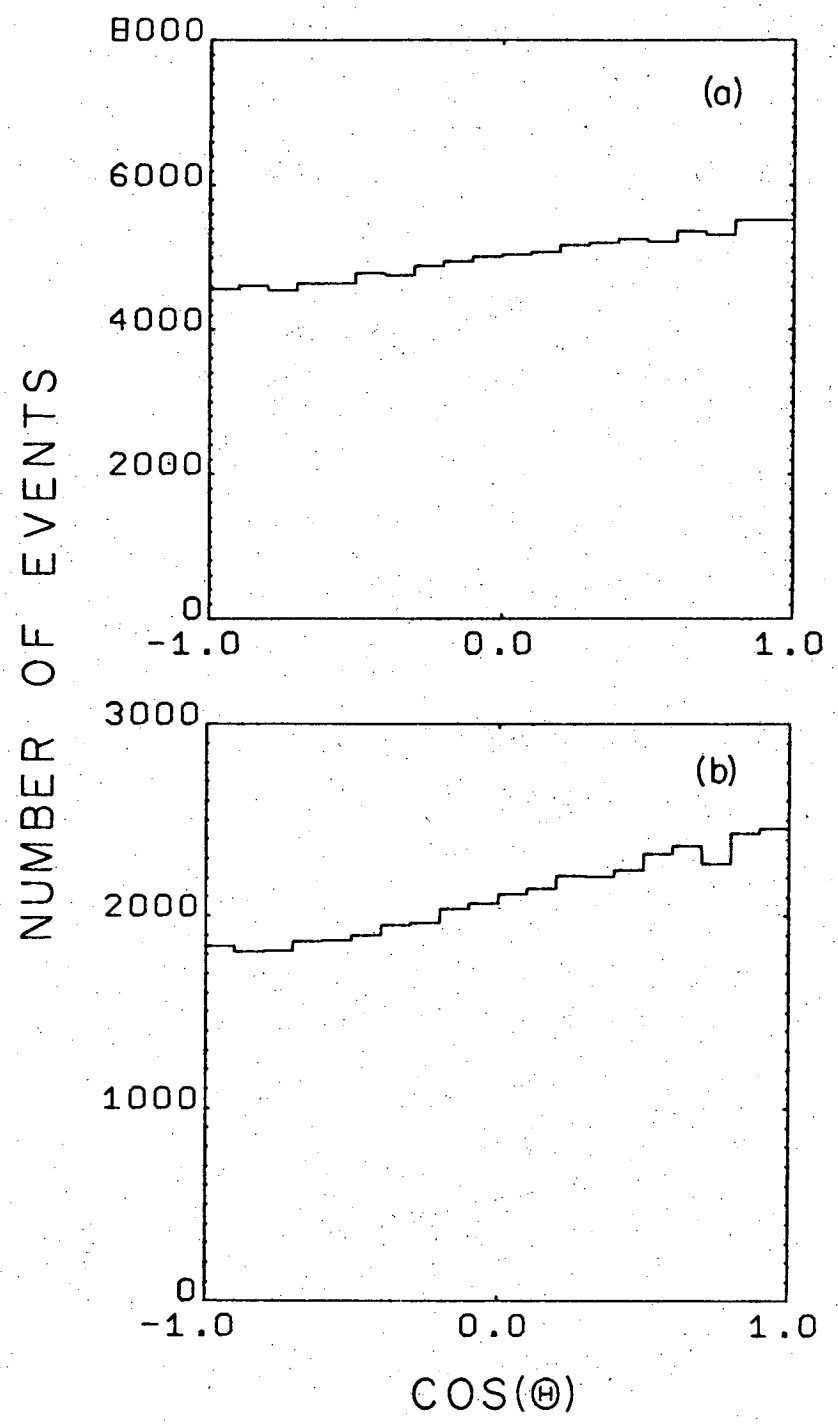

Fig. 32 Prediction of impulse model for angle of spectator with respect to beam for 2.0 GeV/c π beam. a) all spectator momentum b) spectators above 80 MeV/c.

where the model predicts 1-2% of the nucleons should have momenta above 300 MeV/c, we find 15%. See fig. 33 for two examples. Although it is difficult to make a quantitative prediction, the discrepancy can be qualitatively explained by reactions outside of the realm of the impulse approximation, reactions involving both nucleons. Although the nucleons are loosely bound, the nucleons spend a certain amount of time close together, at which time the incoming beam could interact with both simultaneously. Also, after interacting with one of the nucleons, the outgoing particles are within a couple of fermis of the nucleon, and there is a few percent probability of rescattering. Both of these mechanisms result in fast, forward-going nucleons, and probably are the cause of the excess of high momentum nucleons.

One could try to extract nucleon cross sections from an analysis of the c.m. energy distribution, using one of the deuteron wave functions, correcting for the effect of screening of one nucleon by the other (Glauber correction[18]), and attempting to account for the high momentum nucleons. If possible, however, a better procedure would be to compare the c.m. energy distribution of the reaction of interest to one whose cross section is known, making cuts on spectator momentum in both reactions to eliminate high momentum spectators. If both have the same general distributions in spectator momentum then this process should result in a rather good determination of the cross section. For example, suppose we have the reactions

$$\pi^+ n \rightarrow p\pi^+\pi^-$$

and

$$\pi^+ n \rightarrow p\omega$$

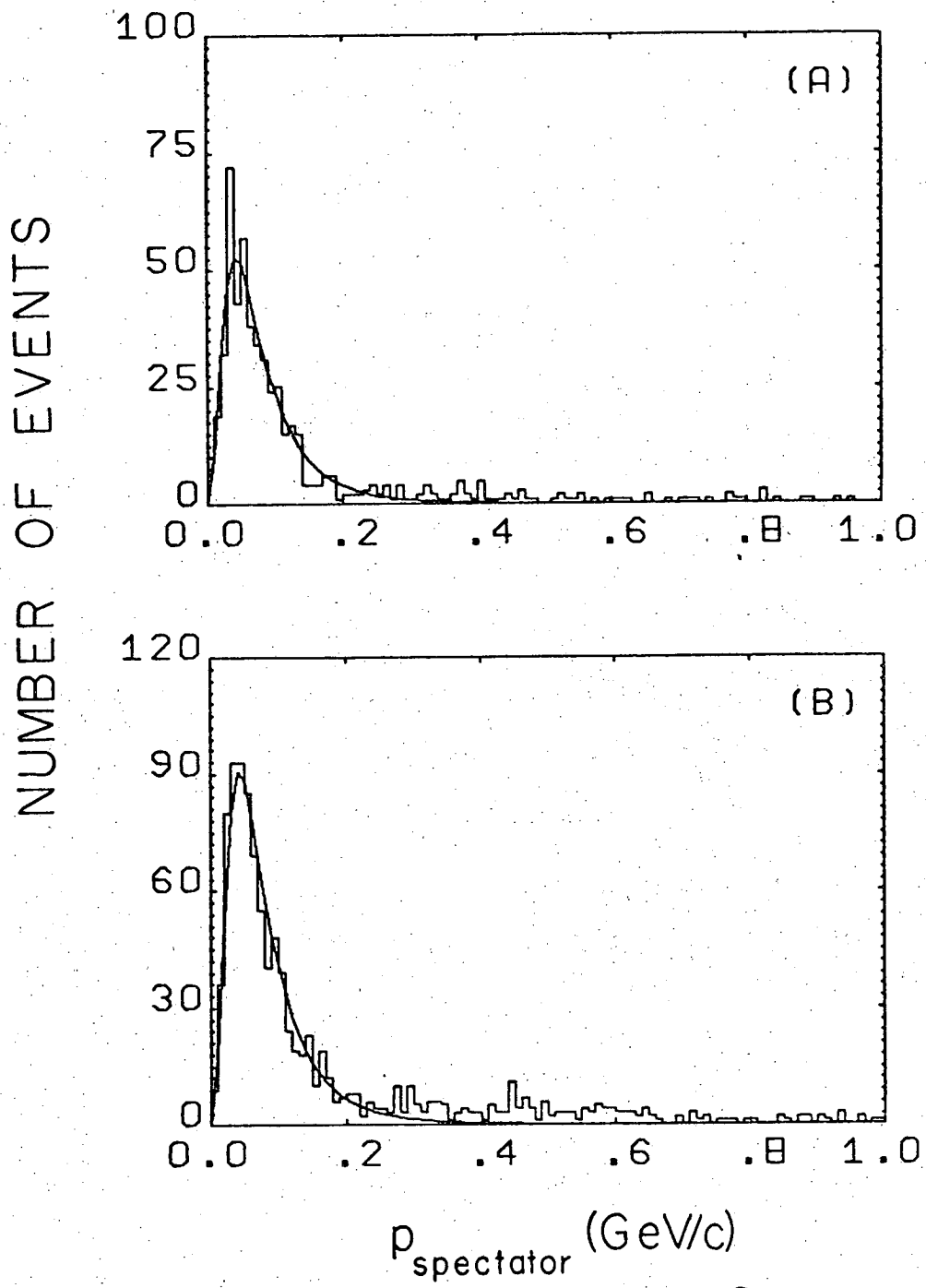

Fig. 33 Spectator momentum distributions. a) Neutron laboratory momentum distribution for $n\Lambda K^+\pi^+$ final state. b) Proton laboratory momentum distribution for $p\Lambda K^+$ final state. Curves are Hulthen wave function predictions normalized to have same area as histogram below 200 MeV/c. a) has 13% of its nucleons above 300 MeV/c b) has 16%.

and we want the cross section for the latter. If we know the cross section for

$$\pi^- p \rightarrow n\pi^+\pi^-$$

we can invoke charge symmetry to equate this to the first reaction. Making identical cuts on spectator momentum we can then just take the ratio of the number of events in the $p\omega$ channel to that in the $p\pi^+\pi^-$ channel to get the cross section.

For other physical quantities (production and decay distributions, invariant mass distributions, etc.) there is much less of a problem. As long as the events are restricted to those for which the impulse approximation appears to be valid, i.e. low momentum nucleons, the physics obtained should be that of the interaction with a nucleon.

B. The Rho-photon Analogy

Consider the diagram shown in fig. 34(a). The amplitude for this diagram will be the product of an upper vertex factor and a lower vertex factor divided by the rho propagator. The properties of the upper vertex are just those of $\rho \longrightarrow \pi\pi$. In general, however there are three ways of coupling at the lower vertex (just the number of ways to couple a $\frac{1}{2}^+$ particle, a 1^- particle, and orbital angular momentum to get a $\frac{3}{2}^+$ particle). The ρ-photon analogy is a model relating the lower vertex to photoproduction of a pion at a c.m. energy near the $\Delta(1236)$ mass. (Fig. 34(b))

Since the Δ has an isospin of $\frac{3}{2}$ it will be the isovector part of the photon that participates in the reaction; this part can be thought of as being mediated by the ρ-meson. (Fig. 34(c))

This vertex is exactly the same as the lower vertex in fig. 34(a) and we can use the properties of the photoproduction amplitude to get the lower vertex factor.

The experimental properties of the photoproduction amplitude are well described by saying that the reaction goes by an M1 transition

$$\gamma_{M1} + p \longrightarrow \Delta^+ \longrightarrow p + \pi^o \quad (\text{ p-wave }).$$

The wave function for the M1 photon will be denoted as $\xi_{\pm 1}$ depending on the projection of its angular momentum along its line of flight (z-axis). What final $J = \frac{3}{2}$ states does each projection give when combined with a nucleon?

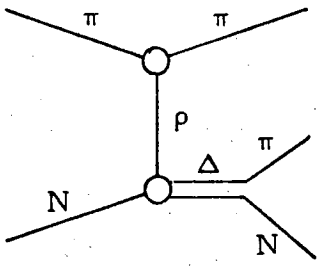

(a)

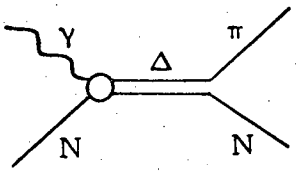

(b)

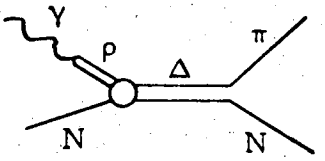

(c)

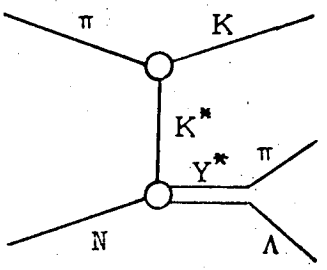

(d)

Fig. 34 Feynman diagrams for a) Δ production by ρ-exchange, b) photoproduction of a pion at a c.m. energy corresponding to the Δ(1236) mass, c) same as b) but mediated by the ρ-meson, d) $Y^*(1385)$ production by $K^*(890)$ exchange.

$$\begin{array}{lll} (\ \gamma\text{-N state}\ ) & \Delta & (\ \pi\text{-N state}\ ) \\ \xi_{+1}\left|\tfrac{1}{2}\ \tfrac{1}{2}\right\rangle \longrightarrow & \left|\tfrac{3}{2}\ \tfrac{3}{2}\right\rangle \longrightarrow & Y_1^1 \chi_{+\frac{1}{2}} \\ \xi_{-1}\left|\tfrac{1}{2}\ \tfrac{1}{2}\right\rangle \longrightarrow & \sqrt{\tfrac{1}{3}}\left|\tfrac{3}{2}\ -\tfrac{1}{2}\right\rangle \rightarrow & \sqrt{\tfrac{1}{3}}\left\{\sqrt{\tfrac{2}{3}}Y_1^0\chi_{-\frac{1}{2}} + \sqrt{\tfrac{1}{3}}Y_1^{-1}\chi_{+\frac{1}{2}}\right\} \end{array}$$

If the initial photon is unpolarized, then the final angular distribution will be just the incoherent sum of the states arising from the ± 1 projections of the M1 photon

$$|\psi|^2 = \frac{1}{2}\left\{|Y_1^1|^2 + \frac{1}{3}\left(\frac{2}{3}|Y_1^0|^2 + \frac{1}{3}|Y_1^{-1}|^2\right)\right\}$$
$$= \frac{1}{24\pi}(5 - 3\cos^2\theta)$$

This is the photoproduction angular distribution for <u>unpolarized</u> photons. However in the reaction given in fig. 34(a) the ρ will have its "polarization vector"* in the production plane. If we take the y-axis as the normal to the production plane (coordinate system of fig. 21), then we want to calculate the photoproduction distribution for photons polarized in the x-direction. The photon wave function will then be a coherent combination of the two M1 wave functions; the correct combination is

$$\psi_x = \sqrt{\frac{1}{2}}\ (\xi_{+1} + \xi_{-1}).$$

Taking this, squaring it, and expressing it in terms of the π-nucleon final state we get

$$|\psi|^2 = \frac{1}{2}\left\{\left|Y_1^1 + \frac{1}{3}Y_1^{-1}\right|^2 + \frac{2}{9}|Y_1^0|^2\right\}$$
$$= \frac{1}{24\pi}\ (5 - 3\cos^2\theta - 3\sin^2\theta\cos 2\phi)$$

---

* Note the use of the words "polarization vector". When applied to a spin-1 particle other than a photon, this should be called "state vector".

This then, by the ρ-photon analogy is what we predict for the Δ decay distribution for the reaction in fig. 34(a). Invoking SU_3 it is also what we expect for the Y^* decay distribution in

$$\pi^+ + p \longrightarrow Y^{*+} + K^+$$

by $K^*(890)$ exchange (Fig. 34(d)).

In terms of the $J=\frac{3}{2}$ spin density matrix elements, the predictions are

$$\rho_{33} = \frac{3}{8}$$

$$\mathrm{Re}(\rho_{31}) = 0$$

$$\mathrm{Re}(\rho_{3-1}) = \frac{\sqrt{3}}{8}$$

We can also make predictions about the isobar production distribution. Writing the linearly polarized M1 photon in terms of the photon's intrinsic polarization and orbital angular momentum we get

$$\psi_x = Y_1^0(k)\epsilon_x$$

where $\vec{k}$ is the photon's momentum vector and $\vec{\epsilon}$ is its polarization vector. However $Y_1^0(k)=k_z$ and the expression for ψ_x reduces to

$$\psi_x = k_z \epsilon_x$$

$$= \vec{k} \times \vec{\epsilon}$$

since $\vec{k}$ has only a z-component and $\vec{\epsilon}$ only an x-component.

Remembering that

$$\vec{k} = \vec{p}_\pi - \vec{p}_K$$

$$\vec{\epsilon} = \vec{p}_\pi + \vec{p}_K$$

we get

$$|\psi_x|^2 = |\vec{p}_\pi \times \vec{p}_K|^2$$

Up to this point all quantities have been evaluated in the isobar's rest frame. Transforming to center of mass quantities one can show that

$$|\vec{p}_\pi \times \vec{p}_K|^2 = C|\vec{P}_\pi \times \vec{P}_K|^2$$

where $\vec{P}_\pi$, $\vec{P}_K$ are the momentum of the π, K in the overall center of mass and C is independent of production angle. Dividing by the K^* propagator we get the production distribution in the overall center of mass

$$\frac{d\sigma}{d\Omega} \propto \frac{\sin^2\Theta}{(t - m_K^{2*})^2}$$

where Θ is the production angle and t the momentum transfer from the π to the K.

REFERENCES

1. O. Dahl et al., Phys. Rev. 163, 1377 (1967).
2. O. Dahl et al., Phys. Rev. 163, 1430 (1967).
3. Bevatron Experimenters Handbook, Lawrence Radiation Laboratory, (Dec., 1965). This beam is referred to as secondary beam 1B.
4. P. Hoch, Lawrence Radiation Laboratory Alvarez Group Physics Note No. 616, 1967.
5. A. A. Carter et al., Phys. Rev. 168, 1457 (1968).
6. For the cross section in our center of mass energy range, see L. D. Jacobs, UCRL-16877, E. West, et al., Phys. Rev. 149, 1089 (1966), T. C. Bacon et al., Phys. Rev. 157, 1263 (1967), J. Alitti, et al., Nuovo Cimento 29, 515 (1963), and E. Pickup et al., Phys. Rev. 132, 1819 (1963).
7. J. Danburg and G. Lynch, Lawrence Radiation Laboratory Alvarez Programming Group Note No. P-160.
8. S. Dagan et al., Phys. Rev. 161, 1384 (1967).
9. H. Foelsche et al., Paper submitted to the 1964 International Conference on High Energy Physics at Dubna.
10. A. Donnachie et al., Phys. Letters, 26B, 161 (1968).
11. L. Stodolsky and J. J. Sakurai, Phys. Rev. Letters 11, 90 (1963).
12. L. Stodolsky, Phys. Rev. 134, B1099 (1964).
13. P. Hoch, Lawrence Radiation Laboratory, private communication.
14. R. Bland, Single pion production in the K^+p channel from 860 to 1360 MeV/c (PhD. thesis), UCRL-18131 (March 1968).
15. G. Gidal et al., Evidence concerning ρ-exchange in the reactions $\pi^+p \to \pi^o\Delta^{++}$ and $\pi^+p \to \omega^o\Delta^{++}$, UCRL-18351 (July 1968).

16. J. Danburg, Lawrence Radiation Laboratory, private communication.

17. V. Franco and R. J. Glauber, Phys. Rev. 142, 1195 (1966).

18. R. J. Glauber, Phys. Rev. 100, 242 (1955).

TECHNICAL INFORMATION DIVISION
LAWRENCE RADIATION LABORATORY
UNIVERSITY OF CALIFORNIA
BERKELEY, CALIFORNIA 94720